# The export flux of particulate organic carbon derived from $^{210}Po/^{210}Pb$ disequilibria along the North Atlantic GEOTRACES GA01 transect: GEOVIDE cruise

Yi Tang[1,2], Nolwenn Lemaitre[3], Maxi Castrillejo[4,5], Montserrat Roca-Martí[5,6], Pere Masqué[5,7], Gillian Stewart[2,1]

[1] Earth and Environmental Sciences, the Graduate Center, City University of New York, New York, USA
[2] School of Earth and Environmental Sciences, Queens College, City University of New York, Flushing, USA
[3] Department of Earth Sciences, Institute of Geochemistry and Petrology, ETH-Zürich, Zürich, Switzerland
[4] Laboratory of Ion Beam Physics, ETH-Zürich, Otto Stern Weg 5, Zürich, 8093, Switzerland
[5] Institut de Ciència i Tecnologia Ambientals and Departament de Física, Universitat Autònoma de Barcelona, Barcelona, Spain
[6] Woods Hole Oceanographic Institution, Woods Hole, MA 02543, USA
[7] School of Science and Centre for Marine Ecosystems Research, Edith Cowan University, Joondalup, Western Australia, Australia

*Correspondence to*: Gillian Stewart (Gillian.Stewart@qc.cuny.edu)

**Abstract**

The disequilibrium between $^{210}$Po activity and $^{210}$Pb activity in seawater samples was determined along the GEOTRACES GA01 transect in the North Atlantic during the GEOVIDE cruise (May – June 2014). A steady-state model was used to quantify vertical export of particulate $^{210}$Po. Vertical advection was incorporated into one version of the model using time-averaged vertical velocity, which had substantial variance. This resulted in large uncertainties for the $^{210}$Po export flux in this model, suggesting that those calculations of $^{210}$Po export fluxes should be used with great care. Despite the large uncertainties, there is no question that the deficits of $^{210}$Po in the Iberian Basin and at the Greenland Shelf have been strongly affected by vertical advection. Using the export flux of $^{210}$Po and the particulate organic carbon (POC) to $^{210}$Po ratio on total (> 1 μm) particles, we determined the POC export fluxes along the transect. Both the magnitude and efficiency of the estimated POC export flux from the surface ocean varied spatially within our study region. Export fluxes of POC ranged from negligible to 10 mmol C $m^{-2}$ $d^{-1}$, with enhanced POC export in the Labrador Sea. The cruise track was characterized by overall low POC export relative to net primary production (export efficiency < 1-15%); but relatively high export efficiencies were seen in the basins where diatoms dominated the phytoplankton community. The particularly low export efficiencies in the Iberian Basin, on the other hand, were explained by the dominance of smaller phytoplankton, such as cyanobacteria or coccolithophores. POC fluxes estimated from the $^{210}$Po/$^{210}$Pb and $^{234}$Th/$^{238}$U disequilibria agreed within a factor of 3 along the transect, with higher POC estimates generally derived from $^{234}$Th. The differences were attributed to integration timescales and the history of bloom events.

## 1. Introduction

The oceans play an essential role in the regulation of atmospheric $CO_2$ and the buffering of the global climate system (e.g. Sabine, 2004) by removing carbon from the atmosphere via dissolution and photosynthesis in the surface ocean, and storing it in the dissolved or particulate forms. An important component of this oceanic sequestration is the biological carbon pump, driven by sinking particles from the surface to the deep ocean (e.g. Falkowski et al., 1998; Ducklow et al., 2001).

The magnitude of particulate organic carbon (POC) export flux from the upper ocean was traditionally obtained from time-series sediment traps (e.g. Honjo et al., 2008) and the natural radiotracer pair, $^{234}$Th/$^{238}$U (e.g. Bhat et al., 1968; Buesseler et al., 1992). Here we focus on the application of another natural radionuclide pair: polonium-210 ($^{210}$Po, $T_{1/2}$ = 138.4 d) and its progenitor lead-210 ($^{210}$Pb, $T_{1/2}$ = 22.3 y). The $^{210}$Po/$^{210}$Pb pair has a different particle-binding dynamic compared to the $^{234}$Th/$^{238}$U pair since both isotopes are particle-reactive, whereas $^{238}$U is conservative and remains dissolved in seawater (Djogic et al., 1986). However, the nature of the particle association differs between the isotopes. Lead-210 and $^{234}$Th are only adsorbed to particle surfaces, whereas $^{210}$Po is both adsorbed to surfaces and biologically reactive so can be assimilated by organisms and even bioaccumulated (Fisher et al., 1983; Cherrier et al., 1995; Stewart and Fisher, 2003a; 2003b). This behavior leads to a higher partitioning coefficient (relative association between the isotope and the particulate vs. the dissolved phase) of $^{210}$Po compared to that of $^{210}$Pb (e.g. Masqué et al., 2002; Wei et al., 2014; Tang et al., 2017).

Lead-210 in the water column comes both from atmospheric deposition and in situ production via the decay of $^{226}$Ra. The residence time of $^{210}$Pb in the atmosphere is only days to weeks (Moore et al., 1974; Turekian et al., 1977). Polonium-210 (produced by decay of $^{210}$Pb via $^{210}$Bi) activities in aerosols, and the subsequent fluxes to the surface ocean, are only about 10 – 20% those of $^{210}$Pb (Masqué et al., 2002). The large difference in their particle reactivity-and half-lives often leads to a disequilibrium between $^{210}$Po and $^{210}$Pb activities in the upper water column as particles sink.

This deviation from secular equilibrium, often in the form of a deficit of $^{210}$Po activity with respect to $^{210}$Pb activity, can be used to estimate POC export in a similar manner to the application of the $^{234}$Th/$^{238}$U disequilibrium (Friedrich and Rutgers van der Loeff, 2002; Verdeny et al., 2009; Wei et al., 2011). Particle export fluxes estimated from the $^{234}$Th/$^{238}$U and the

$^{210}Po/^{210}Pb$ disequilibria integrate export that has occurred on time scales of weeks to months prior to the sampling time, respectively. The use of both isotope pairs could provide complementary information on the causes, timing, and efficiency of export fluxes of POC (e.g. Murray et al., 2005; Stewart et al., 2007; Roca-Martí et al., 2016).

In this study along the GEOTRACES GA01 transect in the North Atlantic, we first used a traditional scavenging model with the assumptions of steady state and negligible physical transport to derive $^{210}Po$ fluxes over different depths of the water column at 11 stations. Then, vertical advection (primarily upwelling) was considered, and its impact on $^{210}Po$ flux was assessed. Using the POC concentration, and particulate $^{210}Po$ activity in the particles collected by in situ pumps, sinking fluxes of POC were then calculated. The magnitude and efficiency of carbon export derived from the $^{210}Po/^{210}Pb$ disequilibrium was considered in relation to the composition of the phytoplankton community. Finally, the POC export fluxes estimated from $^{210}Po/^{210}Pb$ disequilibria were compared with those derived from $^{234}Th/^{238}U$ disequilibria.

## 2. Methods

### 2.1. Cruise track and hydrographic setting

The GEOVIDE cruise (GEOTRACES GA01 transect) was carried out in May - June 2014 from Lisbon to Newfoundland (Fig. 1). Seawater and particulate samples for $^{210}Po$ and $^{210}Pb$ activity analysis were collected from the water column at 11 stations (Fig. 1). The GA01 transect can be separated into five sections according to their biogeochemical characteristics, described in detail by Lemaitre et al., (2018). From east to west, these are: the Iberian Basin (stations 1, 13), the Western European Basin (stations 21, 26), the Iceland Basin (stations 32, 38), the Irminger Basin (stations 44, 60), and the Labrador Basin (stations 64, 69, 77).

### 2.2. Radionuclides sampling and analysis

Radionuclide data were produced by two collaborating laboratories to ensure higher counting statistics for $^{210}Po$ activity in the samples: the Laboratori de Radioactivitat Ambiental at Universitat Autònoma de Barcelona (UAB) (samples from stations 1, 13, and 21) and the Stewart Laboratory at Queens College (QC) (samples from stations 26, 32, 38, 44, 60, 69, and 77). The sampling method for total and particulate $^{210}Po$ and $^{210}Pb$ samples and the determination of the radionuclides activities were described in Tang et al., (2018). In brief, water samples (5 – 10 L

each) for total $^{210}$Po and $^{210}$Pb activity were collected using Niskin bottles at 10 full water column stations (16 – 22 depths/station) and at 1 station to 1000 m (9 depths), for a total of 200 samples. Particulate $^{210}$Po and $^{210}$Pb were collected at 3 – 10 depths per station between 15 and 800 m by using McLane *in-situ* pumps equipped with a 53 μm PETEX screen to capture the large size particles and a 1 μm quartz fiber QMA filter to capture small particles. The average equivalent volume filtered for particulate $^{210}$Po and $^{210}$Pb samples through the PETEX screen was 200 L and through the QMA filter was 70 L.

For water samples, Po and Pb isotopes (including the added chemical yield tracers of $^{209}$Po and stable lead) were co-precipitated with cobalt-ammonium pyrrolidine dithiocarbamate (Co-APDC) (Fleer and Bacon, 1984) at sea, but digested using concentrated HCl and $HNO_3$ back at the home laboratories. Particulate samples were spiked with $^{209}$Po and stable lead before acid digestions (UAB: $HNO_3$/HCl/HF, QC: $HNO_3$/HCl). Polonium isotopes ($^{209}$Po and $^{210}$Po) were plated by deposition onto a sliver disc (Flynn, 1968) and their activities were determined by alpha spectrometry. After removing any remaining Po isotopes by running the plating solution through an anion exchange column, the solution was respiked with $^{209}$Po and stored for at least 6 months. Lead-210 activity was determined by plating the ingrowth of $^{210}$Po from $^{210}$Pb.

The activities of $^{210}$Po and $^{210}$Pb at the sampling date were determined by correcting for nuclide decay, ingrowth, chemical recoveries, detector backgrounds, and blank contamination (Rigaud et al., 2013).

### 2.3. The $^{210}$Po flux method

The export flux of $^{210}$Po was estimated from total $^{210}$Po and $^{210}$Pb activities using a one-box model (Broecker et al., 1973; Matsumoto, 1975; Savoye et al., 2006). The $^{210}$Po activity in the surface ocean is the result of a balance between atmospheric input, continuous production from the decay of $^{210}$Pb in seawater, radioactive decay of $^{210}$Po, removal onto sinking particles, and transport into or out of the box by advection and diffusion. Therefore, the general form of the mass balance equation for $^{210}$Po between sources and sinks is:

$$\partial Po/\partial t = F_{Po} + \lambda_{Po} I_{Pb} - \lambda_{Po} I_{Po} - P + V, \qquad \text{Eq. (1)}$$

where $\partial Po/\partial t$ is the change in $^{210}$Po activity with time, $F_{Po}$ (dpm m$^{-2}$ d$^{-1}$) is the atmospheric flux of $^{210}$Po to the sea surface, $\lambda_{Po}$ is the decay constant of $^{210}$Po (0.005 d$^{-1}$), $I_{Pb}$ and $I_{Po}$ (dpm m$^{-2}$) are the inventories of $^{210}$Pb and $^{210}$Po activities, respectively, $P$ (dpm m$^{-2}$ d$^{-1}$) is the removal flux of $^{210}$Po via sinking particles, and $V$ (dpm m$^{-2}$ d$^{-1}$) is the sum of the advective and diffusive fluxes.

The atmospheric flux of $^{210}$Po is usually ignored as it represents only ~ 2% of the in-situ production of $^{210}$Po from $^{210}$Pb in the upper water column of the open ocean (e.g. Cochran, 1992; Masqué et al., 2002; Murray et al., 2005; Verdeny et al., 2008). We first used a steady state (SS) model that assumes the negligible atmospheric input of $^{210}$Po activity and ignores advection and diffusion. In this case, the $^{210}$Po flux ($P$) can be simplified as follows:

$$P = \lambda_{Po}(I_{Pb} - I_{Po}). \qquad \text{Eq. (2)}$$

The influences of advection and non-steady state (NSS) processes on the overall $^{210}$Po activity balance are discussed below in sections 4.1 and 4.2, respectively.

Many previous studies have used a single fixed integration depth for export calculations at all sampling locations (e.g. 100 m in the Antarctic Circumpolar Current, Rutgers van der Loeff et al., 1997; 120 m in the central Equatorial Pacific, Murray et al., 2005). The GA01 transect, however, crossed diverse physical and biogeochemical conditions. Thus, investigating export at a single fixed depth for every station may bias the spatial comparisons of particle export. In this study, four site-specific integration depths were used for each station: the mixed layer depth (MLD), the depth of the euphotic zone ($Z_{1\%}$), the primary production zone (PPZ), and the $^{234}$Th-$^{238}$U equilibrium depth (ThEq). MLD was defined as a change in potential density of 0.03 kg m$^{-3}$ relative to the potential density at 10 m (Weller and Plueddemann, 1996). $Z_{1\%}$ was defined as the depth where photosynthetic available radiation was 1% of its surface value (Jerlov, 1968). PPZ was the depth at which the fluorescence reaches 10% of its maximum (Owens et al., 2015). ThEq was the depth at the bottom of the total $^{234}$Th water column deficit, where the activity of $^{234}$Th equals that of $^{238}$U (data from Lemaitre et al., 2018). These depths were used both to calculate $^{210}$Po and POC export and in order to compare the POC export fluxes estimated from the $^{210}$Po/$^{210}$Pb disequilibria to those derived from the $^{234}$Th/$^{238}$U disequilibria. Among the 11 stations, the depths of the MLD (23 ± 7 m) were similar to those at $Z_{1\%}$ (31 ± 9 m), whereas the

depths of the PPZ (72 ± 29 m) and ThEq (95 ± 43 m) were deeper and comparable to each other. For the depths of MLD, $Z_{1\%}$, PPZ, and ThEq at which total radionuclides data are not available, the measured values of total $^{210}$Po and $^{210}$Pb activities were linearly interpolated (Table 1).

The $^{210}$Po flux was then used to derive the flux of POC by multiplying the deficit of $^{210}$Po by the ratio of POC concentration to $^{210}$Po activity (POC/$^{210}$Po) of the total particulate material. Particulate $^{210}$Po and POC data were not always available at the depths of the MLD, $Z_{1\%}$, PPZ, and ThEq at our study sites. To estimate POC/$^{210}$Po ratios at these depths, a regression was performed between the measured POC/$^{210}$Po ratios and depth for each basin using a single power law function.

### 2.4. Quantification of the influence of the vertical advection on $^{210}$Po export

Cyclonic/anticyclonic eddies constantly impact the horizontal velocity fields at our study sites (Zunino et al., 2018), changing the current directions and making it difficult to estimate the magnitude of horizontal velocities. This constant variability, together with the patchiness of sampling resolution, meant we could not assess the influence of horizontal advective processes on $^{210}$Po export estimates.

However, because we had relatively high depth resolution at each station, we did attempt to assess the influences of vertical advection on $^{210}$Po inventories at all the investigated depths by measuring the vertical gradient of $^{210}$Po activity and multiplying it by a time-averaged vertical velocity. Because the water column inventory of $^{210}$Po represents an integration of the changes over approximately the mean life of the isotope, we did not use the vertical velocity measured by the acoustic doppler current profiler (ADCP) at the sampling time, but a time-averaged vertical velocity from the Estimating the Circulation and Climate of the Ocean, Phase II (ECCO2). The activity gradient of $^{210}$Po below the depth z (i.e., the MLD, z1%, PPZ, and ThEq) at each station was calculated from the depth $z$ (using the average activity in the layer of 0-$z$ m) as starting point ($A_{Po}^{1}$) and linearly interpolated through the measurements 20 m below $z$ ($A_{Po}^{2}$) at each station. A positive gradient ($A_{Po}^{2}$- $A_{Po}^{1}$ > 0) was defined as higher activity at the depth of ($z$ + 20 m) than the starting point. We labeled the vertical velocity as $w_{20}$ which was the 30-day (30 days prior to the sampling date) average vertical velocity between the depths of z and ($z$ + 20 m). The flux of $^{210}$Po due to vertical advection ($F_w$) was calculated as the following:

$$F_w = w_{20} \times (A_{Po}^2 - A_{Po}^1). \qquad \text{Eq. (3)}$$

Total $^{210}$Po fluxes at each depth, therefore, are the sum of the steady state values based only on the $^{210}$Po deficit (Eq. 2), $\lambda_{Po}(I_{Pb} - I_{Po})$, and vertical advective flux (Eq. 3), $w_{20} \times (A_{Po}^2 - A_{Po}^1)$.

The ECCO2 vertical velocities were obtained from the Asia-Pacific Data-Research Center (APDRC, http://apdrc.soest.hawaii.edu/las/v6/dataset?catitem=1). The ECCO2 model configuration uses a cube-sphere grid projection with 18-km horizontal grid spacing and 50 vertical levels among which there are 12 equal vertical layers from the surface to 120 m (Menemenlis et al., 2008). We selected the ECCO2 grid points closest to the station and extracted vertical velocities from the depths between $z$ and ($z$ + 20 m) during 30 days prior to the sampling date at each station. Because the deficit of $^{210}$Po activity in the water column weighs the changes that occurred shortly prior to the sampling time more heavily than those that occurred further back in time (Verdeny et al., 2009), we chose to average the vertical velocity over one month rather than over the mean life of $^{210}$Po (200 days). The 30-day averaged vertical velocity was then used to calculate vertical advective $^{210}$Po export flux via Eq. (3) at each station.

### 2.5. Satellite-based net primary production and phytoplankton composition

The 8-day net primary production (NPP) data with a spatial resolution of 0.083º by 0.083º were obtained from the Oregon State University Ocean Productivity standard products (http://www.science.oregonstate.edu/ocean.productivity/), wherein NPP was estimated by the Vertically Generalized Production Model (VGPM) (Behrenfeld and Falkowski, 1997). Due to some missing data between November 2013 and February 2014, NPP for each station was averaged for the previous 138 days ($^{210}$Po half-life) instead of 200 days ($^{210}$Po mean life).

Monthly average concentrations of diatoms, coccolithophores, cyanobacteria, chlorophytes, and total chlorophyll with the spatial resolution of 0.67 × 1.25º were obtained from the Goddard Earth Science Data and Information Services Center Interactive Online Visualization and Analysis Infrastructure ("Giovanni") (https://giovanni.gsfc.nasa.gov/giovanni/, Acker and Leptoukh, 2007). Time-series (October 2013 – July 2014, covering > 200 days before sampling) data are averages over longitude for each month. We extracted data for the 5 basins individually and calculated the fraction of each phytoplankton group at each station as the ratio of their concentration to total chlorophyll concentration.

## 3. Results

### 3.1. Satellite-derived seasonal NPP and phytoplankton composition

The VGPM modeled NPP data along the GA01 transect was averaged over ~ 138 days prior to the sampling date (see section 2.5, Table 1). Seasonal NPP at each station varied from low values of 44 – 79 mmol C $m^{-2}$ $d^{-1}$ to a maximum value of 109 mmol C $m^{-2}$ $d^{-1}$ at station 21. The Western European Basin had the highest seasonal NPP, followed by the Iberian Basin; while the Iceland Basin, the Irminger Basin, and the Labrador Basin all had similar NPP values in the range of 45 – 49 mmol C $m^{-2}$ $d^{-1}$. There was a shift in the biological community towards larger phytoplankton (e.g. diatoms) from east to west along the transect (Fig. 2). The basins where diatoms were the dominant phytoplankton group did not necessarily have higher seasonal production relative to the basins where smaller phytoplankton (e.g. coccolithophores) were more abundant. Indeed, the Iberian Basin had the second highest seasonal NPP, despite the fact that the majority of chlorophyll was produced by coccolithophores. Despite the evidence that earlier blooms may have been driven by diatoms (see section 4.2), these observations highlight the possible contribution of small particles to production, and possibly to export (proportional to their role in production according to Richardson and Jackson, 2007) along the transect. Moreover, this could be also due to shorter blooms in the Irminger and Labrador Basins where the phytoplankton growth was light-limited during winter compared to the conditions in the Iberian and Western European Basins.

The satellite-derived phytoplankton species composition demonstrated unique features within the basins (Fig. 2). The Iberian Basin was dominated (> 60%) by coccolithophores between October 2013 – July 2014, but had a gradual increase in the contribution of diatoms until April 2014 and a decreasing contribution after that. In the Western European Basin, station 26 was dominated by diatoms all year around while station 21 was dominated by diatoms except in October 2013 and July 2014 when the combination of chlorophytes and coccolithophores contributed 35 – 77 % to ~~of~~ the total chlorophyll concentration. The stations in the Iceland, Irminger, and Labrador Basins were all dominated (> 98%) by diatoms between October 2013 and July 2014.

### 3.2. One-month averaged vertical velocity $w_{20}$

The one-month averaged vertical velocities $w_{20}$ ranged from -36 × $10^{-6}$ to 9 × $10^{-6}$ m $s^{-1}$ along the transect (negative: upwelling, positive: downwelling, Table 1). The standard deviations of $w_{20}$ were generally of the same order as the values of $w_{20}$. Particularly large standard deviations, which exceed the typical values of the vertical velocity by a full order of magnitude, were found at stations 13 (35-55 m, 110-130 m) and station 21 (110-130 m). These high standard deviations suggest that the data of $w_{20}$ should be used with great care. Downwelling was seen at stations 38, 44, 64, and 77 with the velocities in the range of 1 to 9 × $10^{-6}$ m $s^{-1}$. Upwelling was seen at the remaining stations, with highest intensity at station 60 near Greenland (absolute value: 11 – 36 × $10^{-6}$ m $s^{-1}$). The upwelling velocities were roughly equivalent at stations 1, 13, 21, 26, 32, and 69 (absolute value: 1 – 5 × $10^{-6}$ m $s^{-1}$).

### 3.3. Total $^{210}$Po deficits

The vertical profiles of total $^{210}$Po and $^{210}$Pb activity at each station have been described in a companion article (Tang et al., 2018). Here we show the section view of the water column $^{210}$Po deficit (dpm 100 $L^{-1}$), which was calculated as total $^{210}$Pb activity minus total $^{210}$Po activity (Fig. 3). There were small $^{210}$Po deficits in the upper 100 m (including the majority of the depths of MLD, $Z_{1\%}$, PPZ, and ThEq at all stations) at stations 1, 13, and 21, whereas a relatively large excess of $^{210}$Po was observed at 100 – 400 m depth. Station 60 had the highest deficits of $^{210}$Po (~ 8 dpm 100 $L^{-1}$, n = 5) at 40 – 120 m depth. A large surface deficit of $^{210}$Po was found at station 64 (8 dpm 100 $L^{-1}$) and a surface excess was found at station 38 (-3.5 dpm 100 $L^{-1}$). There were positive $^{210}$Po deficits throughout most of the water column at stations in the Irminger and Labrador Basins, whereas large $^{210}$Po excesses (negative deficits) below 100 m were generally seen in the Iberian Basin and Western European Basins. Such $^{210}$Po excess was likely related to the Iberian upwelling, which may have provided a source of $^{210}$Po activity.

### 3.4. The $^{210}$Po flux calculated from the deficit of $^{210}$Po alone

Using the data of total $^{210}$Po and $^{210}$Pb activities, the amount of $^{210}$Po escaping from the surface ocean via particles ("$^{210}$Po fluxes", dpm $m^{-2}$ $d^{-1}$) was calculated using Eq. (2) assuming steady state and ignoring advection and diffusion (Table 2, $^{210}$Po/$^{210}$Pb term). The $^{210}$Po fluxes were negligible or very low at stations 1, 21, and 38. At the other stations the $^{210}$Po fluxes averaged 3.7 ± 1.4, 4.6 ± 2.6, 9.5 ± 4.9, and 14.4 ± 12 dpm $m^{-2}$ $d^{-1}$ at the MLD, $Z_{1\%}$, PPZ, and

ThEq, respectively. The $^{210}$Po fluxes tended to increase with depth at seven out of eleven stations (26, 38, 44, 60, 64, 69, and 77). At the MLD, $Z_{1\%}$ and PPZ, the largest $^{210}$Po fluxes were all found in the Labrador Basin. The other 4 basins had relatively similar $^{210}$Po export fluxes (2.1 – 2.8 dpm m$^{-2}$ d$^{-1}$) at the MLD and $Z_{1\%}$. The West European Basin had much higher $^{210}$Po flux (8.7 dpm m$^{-2}$ d$^{-1}$) relative to that in the Iberian Basin (-0.1 dpm m$^{-2}$ d$^{-1}$) at the PPZ. At the ThEq, on the other hand, the Irminger Sea had the highest $^{210}$Po fluxes followed by the West European Basin. The lowest $^{210}$Po fluxes at all investigated depths were generally found in the Iberian Basin.

### 3.5. POC/$^{210}$Po ratios in particles

Most of the ratios of POC concentration to $^{210}$Po activity (μmol dpm$^{-1}$) in the large size fraction of particles (POC/$^{210}$Po_LSF, > 53 μm) were comparable to or higher than those in the small size fraction (POC/$^{210}$Po_SSF, 1 – 53 μm), although a few samples at stations 13, 26, 44, 64, and 77 had lower values of POC/$^{210}$Po_LSF than those of POC/$^{210}$Po_SSF (Table 3, Fig. 4a). The POC/$^{210}$Po ratio in the total particles (> 1 μm, the combination of small and large particles, POC/$^{210}$Po_TPF) was similar to that in the small particles (SSF), within about 97% (Table 3, Fig. 4b). This is because over 80% of the particulate $^{210}$Po activity was associated with the small size fraction (Tang et al., 2018) likely due to the large surface area of abundant small particles. Because of the possible link between small particles and export along the transect discussed in section 3.1, and the results that scavenging of $^{210}$Po was governed by the small particles (Tang et al., 2018), we propose to use this total particulate fraction in addition to the more commonly used large size fraction to calculate POC export along this cruise track.

The POC/$^{210}$Po in total particles (POC/$^{210}$Po_TPF) varied from 19 to 1300 μmol dpm$^{-1}$ with a mean of 290 ± 320 μmol dpm$^{-1}$ (n = 51, upper 800 m). The variability of POC/$^{210}$Po_TPF ratios in this study is in line with previous observations in the Antarctic Circumpolar Current (300 - 1200 μmol dpm$^{-1}$ for particles > 1 μm) (Friedrich and Rutgers van der Loeff, 2002), and the central Arctic (90 - 1900 μmol dpm$^{-1}$ for particles > 53 μm) (Roca-Martí et al., 2016). The average ratio of 290 μmol dpm$^{-1}$ is comparable to those observed in the central Equatorial Pacific (202 ± 90 μmol dpm$^{-1}$ for particles > 0.45 μm) (Murray et al., 2005), the North Atlantic (290 ± 70 μmol dpm$^{-1}$ for particles > 1 μm) (Rigaud et al., 2015), and the South Atlantic (113 ± 80 μmol dpm$^{-1}$ for particles > 0.7 μm) (Sarin et al., 1999).

The measured POC/$^{210}$Po ratios in total particles at each station and depth were grouped into the 5 basins and fitted against depth using a single power law function in each basin (Fig. 5). The fit equations were used to calculate total particulate POC/$^{210}$Po ratios at the investigated depths at each station (Table 3).

## 4. Discussion

### 4.1. Physical advection effects on $^{210}$Po export fluxes

In the study region, there were consistent patterns of circulation traveling through and near our sampling sites during the GEOVIDE cruise. From east to west the cruise track crossed the North Atlantic Current, the Eastern Reykjanes Ridge Current, the Irminger Current, the Irminger Gyre, the Western and Eastern Boundary Currents and the Labrador Current (Fig. 1 in García-Ibáñez et al., 2018). Additionally, short-lived eddies and fronts were also observed during the cruise, particularly in the OVIDE section from Portugal to Greenland (García-Ibáñez et al., 2018; Zunino et al., 2018). In this dynamic region advective influences may be important to include in calculations of $^{210}$Po export. Despite this knowledge, we could not include horizontal advection in our model because the horizontal resolution of our sample sites was not sufficient to constrain reliable horizontal gradients of $^{210}$Po activity in the study region. This assumption of negligible horizontal physical transport has been made in most $^{210}$Po studies because of a similar lack of spatial resolution (e.g. Kim and Church, 2001; Stewart et al., 2010; Rigaud et al., 2015), and may be justified in some open ocean settings where horizontal gradients in $^{210}$Po activities are small (e.g. Wei et al., 2011). For more dynamic regimes such as along the GA01 transect, however, this assumption needs to be carefully evaluated, and the relative importance of advective $^{210}$Po flux should be assessed if possible.

We did, however, have enough sampling depths at each station to assess the vertical variability in $^{210}$Po activity and to estimate the impact of vertical advection on the $^{210}$Po flux. The range of $^{210}$Po activity flux due to vertical advection (-40 to 14 dpm m$^{-2}$ d$^{-1}$, Table 2) was of the same magnitude as the steady state fluxes calculated from the deficit alone (-5 to 37 dpm m$^{-2}$ d$^{-1}$, Table 2). The magnitude of the uncertainty of the $^{210}$Po export flux due to vertical advection was influenced by the large variance in vertical velocity field mentioned in Sect. 3.2. When excluding the three depths at stations 13 and 21 where the monthly vertical velocity average had substantial standard deviations (an order of magnitude greater than $w_{20}$), the uncertainty of the $^{210}$Po export

flux was on average 2-fold larger than the calculated $^{210}$Po export flux. The largest positive vertical advective $^{210}$Po fluxes were at station 1 where the Iberian upwelling increased the calculated flux by 150 - 500%. The largest negative vertical advective $^{210}$Po fluxes were seen at station 60 where upwelling decreased the $^{210}$Po flux by 370 – 1100% at the depths of the MLD, $Z_{1\%}$, and PPZ. This is because the upwelling velocity was high at those depths (14 – 36 × $10^{-6}$ m $s^{-1}$, Table 1) and the water upwelled was depleted in $^{210}$Po activity. The vertical advective transport was smaller at the MLD and $Z_{1\%}$ at station 13, at the ThEq at station 21, and at the PPZ and ThEq at station 64, with contributions lower than 6% of the total $^{210}$Po fluxes. Including vertical advection in our flux estimates at all other depths, however, increased/decreased the $^{210}$Po fluxes by 10 – 180%. Like with vertical advection, neglecting horizontal advection can result in either an underestimate or overestimate of $^{210}$Po export flux depending on whether the advected water is enriched or depleted in $^{210}$Po. However, because our study region was characterized by distinct water masses separated over 10s to 100s of meter in the vertical plane, whereas those same water masses covered huge distances (100s to 1000s of kilometer) in the horizontal plane (Fig. 4 in García-Ibáñez et al., 2018), vertical advection would most likely result in more change in physical and chemical parameters over the scale of sampling than horizontal advection would. Because the advective $^{210}$Po export flux was calculated as the product of the velocity of the water mass and the gradient of $^{210}$Po activity in the corresponding direction, horizontal advection would most likely contribute a much smaller range of advective $^{210}$Po flux estimates.

Overall, the influence of physical advection on $^{210}$Po activity may range from relatively unimportant to dominant depending on study area. In this study, we observed physical processes influencing $^{210}$Po fluxes, in particular at stations 1 and 60. For future studies of $^{210}$Po and $^{210}$Pb activity in regions of established upwelling or ocean margins, we suggest designing the sampling plan so that the magnitude and variability of these processes may be incorporated into $^{210}$Po export models. At ocean margins, in particular, more water samples should be taken to improve the resolution of horizontal features.

### 4.2. Non-steady state effects on $^{210}$Po export fluxes

To our knowledge, three time-series studies of $^{210}$Po and $^{210}$Pb activities have been conducted to date and have assessed the NSS effects on $^{210}$Po fluxes. First, in the upper 500 m of the

Sargasso Sea, Kim and Church, (2001) found that the SS model may have overestimated and underestimated the $^{210}$Po export fluxes in May and July 1997, respectively. Second, at the DYFAMED site of the northwestern Mediterranean Sea, the $\partial Po/\partial t$ term accounted for ~ 50% of $^{210}$Po flux estimated by using the SS model (Stewart et al., 2007). Last, in the South China Sea, the $^{210}$Po export fluxes at 1000 m calculated from the SS and NSS models had similar values within the uncertainties (Wei et al., 2014). In fact, the SS model generally results in an underestimation of the $^{210}$Po flux under conditions of decreasing $^{210}$Po activities in the water column (i.e. when blooms switch from the productive phase to the export phase) whereas the SS model overestimates the flux for conditions of increasing $^{210}$Po activities (i.e. high atmospheric deposition).

Atmospheric aerosol deposition along the GA01 transect was reportedly low, without significant influence of the Saharan plume (Shelley et al., 2017). The influence of atmospheric deposition on the SS estimates obtained in this study, therefore, can be ignored. However, it is important to assess the $\partial Po/\partial t$ term that was associated with the site-specific bloom events during the cruise. Satellite estimates of net primary production (VGPM model) for the eight 8-day periods prior to the sampling date (~ 2 months) were calculated at each station (Fig. 6). Two months' NPP data is needed because such a time scale could ensure the sensitivity for NSS estimates (Friedrich and Rutgers van der Loeff, 2002; Stewart et al., 2007). NPP for the two-month period were in the ranges of 51 – 184, 39 – 403, 22 – 131, 18 – 204, 16 – 210 mmol C m$^{-2}$ d$^{-1}$ in the Iberian Basin, the West European Basin, the Iceland Basin, the Irminger Basin, and the Labrador Basin, respectively, indicating the occurrence of blooms during this time period along the transect that might have influenced the $^{210}$Po fluxes derived from Eq. (1).

Assuming SS may have underestimated the $^{210}$Po export along the GA01 transect depending on the stage of the bloom before sampling. For example, at station 21 the largest NPP peak (403 mmol C m$^{-2}$ d$^{-1}$) occurred 2 weeks before our sampling date and diminished rapidly (~ 100 mmol C m$^{-2}$ d$^{-1}$ at sampling time). The combination of high phytoplankton export and sudden decrease in NPP may have significantly lowered the $^{210}$Po activity in the upper waters, resulting in a negative $\partial Po/\partial t$, and thus the SS model may have underestimated the true $^{210}$Po flux. Temporal variations were also seen in the time-series phytoplankton community composition, in particular at stations 1 and 13 (Fig. 2). Both stations were dominated (> 60%) by coccolithophores between October 2013 – July 2014, but appeared to have a diatom bloom in April 2014 before sampling.

Polonium-210 and $^{210}$Pb tend to bind to specific biopolymeric functional groups, leading to fractionation during their sorption onto particles (Quigley et al., 2002; Chuang et al., 2013; Yang et al., 2013). The temporal variation of phytoplankton composition could therefore also lead to non-steady state effects on the overall $^{210}$Po activity balance, which are difficult to assess but deserve more attention.

The NSS effect on the $^{234}$Th fluxes at the ThEq were evaluated during the same cruise along the GA01 transect in Lemaitre et al., (2018) by using the NSS model developed in Savoye et al., (2006). Because the cruise plan did not allow an opportunity to reoccupy the study areas over time, the authors made the assumption that $^{234}$Th activity was in equilibrium with $^{238}$U activity at the starting date of the bloom. Their results suggested that the NSS $^{234}$Th fluxes were about 1.1 to 1.3 times higher than the SS estimates in the Iberian and West European Basins, and 1.4 to 2.1 times higher in the Iceland, Irminger, and the Labrador Basins. We did not attempt to apply the same technique to estimate NSS $^{210}$Po fluxes in this study because the assumption of equilibrium between $^{210}$Po activity and $^{210}$Pb activity at the starting date of the bloom may be inappropriate and the $^{210}$Po deficit integrates over a longer time period (months) than a typical bloom event (days/weeks).

### 4.3. POC flux calculated from $^{210}$Po flux

The POC export fluxes were calculated by multiplying both the $^{210}$Po export fluxes calculated from the deficit alone (SS without advection) and the total $^{210}$Po fluxes (sum of the fluxes calculated from the $^{210}$Po deficit and vertical advection) by the total particulate (> 1 μm) POC/$^{210}$Po ratios at the corresponding depths (Table 2, Fig. 7). The POC fluxes calculated from only the deficit term and the total term ranged from negligible to 7 mmol C m$^{-2}$ d$^{-1}$ and from negative to 10 mmol C m$^{-2}$ d$^{-1}$, respectively. This is in good agreement with the SS fluxes derived via the $^{210}$Po/$^{210}$Pb method ignoring advection in other regions of the world ocean (negligible to 8.5 mmol C m$^{-2}$ d$^{-1}$) (e.g. Shimmield et al., 1995; Sarin et al., 1999; Kim and Church, 2001; Stewart et al., 2007; Verdeny et al., 2008; Roca-Martí et al., 2016; Subha Anand et al., 2017).

The highest estimated POC fluxes (Table 2) along the transect were observed at most of the investigated depths in the Labrador Sea and at the Greenland Shelf, whereas the lowest export was in the Iberian and West European Basins. An exception to this pattern was found at station

26 where POC flux was actually similar in magnitude to the flux at stations 64 and 69. Station 26 was located in the middle of the Subarctic Front (SAF), a cold and fresh anomaly originating from subpolar water (Zunino et al., 2018). The hydrographic properties associated with the SAF appear to promote high primary production (174 ± 19 mmol C $m^{-2}$ $d^{-1}$, Table 1) and subsequently high carbon export (Kemp et al., 2006; Rivière and Pondaven, 2006; Guidi et al., 2007; Waite et al., 2016). While stations on the Greenland Shelf (stations 60 and 64) had the greatest estimated carbon export at the depth of ThEq (5 – 10 mmol C $m^{-2}$ $d^{-1}$), station 60 at the depth of $Z_{1\%}$ had the lowest POC flux (-12.5 to -8.4 mmol C $m^{-2}$ $d^{-1}$).

The negligible deficit of $^{210}$Po at the MLD and $Z_{1\%}$ seen at stations 21, 38 and 44 leads to negligible $^{210}$Po-derived POC fluxes at those depths and stations (Table 2, Fig. ~~6~~7). The relatively low POC export (negligible – 1.7 mmol C $m^{-2}$ $d^{-1}$) at stations 1 and 13, on the other hand, resulted from low particulate POC/$^{210}$Po ratios (Table 2). In fact, the Iberian Basin had the lowest measurements of particulate POC/$^{210}$Po ratios in both the small and large size fractions relative to the other four basins along the transect (Fig. 4). This basin was also the only region along the transect where the phytoplankton community was not dominated by diatoms but by smaller phytoplankton, in particular coccolithophores. Smaller phytoplankton cells could scavenge more $^{210}$Po (higher particulate $^{210}$Po activity relative to the large particles) due to larger surface area per unit of volume, lowering their ratio of POC concentration to $^{210}$Po activity.

### 4.4. POC export efficiency

The POC export flux calculated from the total $^{210}$Po flux at the depth of the PPZ was compared to the satellite-derived NPP over ~ 138 days (see section 2.5) at each station, and the ratio was reported as the POC export efficiency.

The export efficiencies in this study were below 10% at 10 out of 11 stations, averaging 6 ± 4% (n = 10, excluding the negative value at station 60, Fig. 8). Export efficiencies < 10% observed here were similar to those found in the Equatorial Pacific, the Arabian Sea, and at the BATS site (Buesseler, 1998; Subha Anand et al., 2017), but lower than those reported at high latitude sites (> 25%) such as the Arctic (Gustafsson and Andersson, 2012; Moran et al., 1997; Roca-Martí et al., 2016), the Bellingshausen Sea (Shimmield et al., 1995), and the Antarctic Polar Front (Rutgers van der Loeff et al., 1997).

Export efficiencies ranged from 0.5 to 2.5% in the Iberian Basin, while the values in the Irminger Basin (3 ± 3%, excluding station 60) were similar to the export efficiencies in the Western European Basin (5 ± 5%) and in the Iceland Basin (6 ± 6%). The export efficiencies, in contrast, were larger in the Labrador Basin (10 ± 3%). The lowest export efficiencies observed in the Iberian Basin were consistent with the dominance of smaller phytoplankton species there (coccolithophores and cyanobacteria; Fig. 2). Indeed, small cells are usually slow-sinking particles that are likely more prone to degradation (Villa-Alfageme et al., 2016), leading to lower export efficiencies. Conversely, the higher export efficiencies at other stations, all generally dominated by diatoms (Fig. 2), support the idea that diatoms may be more efficient in exporting POC than smaller phytoplankton (Buesseler, 1998). Differences in export efficiencies between the basins dominated by diatoms suggest that other factors may also play some role (e.g., temporal decoupling between production and export).

The POC export efficiency could also vary widely within the same basin. Taking the two stations in the Western European Basin for instance, export efficiency at station 26 was ~ 5-fold greater than that estimated at station 21, likely consistent with a lower contribution of diatoms and a higher contribution of smaller phytoplankton at station 21 relative to those at station 26 (Fig. 2). But overall the time-series composition of the phytoplankton community at the two stations was similar (Fig. 2). The site-specific environment may have impacted the export of the same cell type to different degrees (Durkin et al., 2016). Station 26 was in the middle of the SAF, and the mesoscale physical processes (i.e. turbulence and mixing) at the front can introduce nutrients into the local euphotic zone (Lévy et al., 2012). Large phytoplankton species generally dominate in these nutrients-rich waters and can promote massive episodic particle export (e.g. Kemp et al., 2006; Guidi et al., 2007; Waite et al., 2016).

### 4.5. Comparison of $^{210}$Po and $^{234}$Th derived POC fluxes

The measurements of $^{234}$Th/$^{238}$U disequilibrium to estimate POC export flux were simultaneously carried out during the GEOVIDE cruise (Lemaitre et al., 2018). The authors discussed the influence of vertical advection on $^{234}$Th export flux and concluded it can be neglected. In the present study, estimates of $^{234}$Th-derived POC ($^{234}$Th-POC) flux were compared to $^{210}$Po-derived POC ($^{210}$Po-POC) flux. To avoid discrepancies, both the $^{234}$Th-POC and $^{210}$Po-POC flux estimates were calculated at the depth of ThEq using the POC/radionuclide ratio in

total particles > 1 µm (TPF) and large particles > 53 µm (LSF), and both methods ignored physical transport and assumed steady state, where any deviation from secular equilibrium was created by sinking particles with an adsorbed and/or absorbed excess of the short-lived daughter isotope.

#### 4.5.1. $^{210}$Po flux vs. $^{234}$Th flux

The integrated $^{210}$Po and $^{234}$Th fluxes at the depth of ThEq were compared (Fig. 9). There was a spatial trend of $^{234}$Th flux, but not $^{210}$Po flux along the transect; $^{234}$Th fluxes at stations 1 to 38 (eastern section, 1580 ± 430 dpm $m^{-2}$ $d^{-1}$) were significantly greater (Wilcoxon rank sum test, p-value < 0.002) than the fluxes at stations 44 to 77 (western section, 710 ± 230 dpm $m^{-2}$ $d^{-1}$). The means of the $^{210}$Po fluxes in the western and eastern sections were not statistically different from each other (Wilcoxon rank sum test, p-value = 0.3). However, the flux of $^{210}$Po and $^{234}$Th correlated with each other better in the western (n = 5, $R^2$ = 0.6) than in the eastern (n = 6, $R^2$ = 0.01) sections.

These relationships may be related to both the stage of the bloom and different half-lives of the two isotopes. Indeed, $^{234}$Th fluxes integrate the conditions that occurred days to weeks prior to the sampling date while the $^{210}$Po method integrates the flux over the past few months. Within the Iberian Basin, stations 1 and 13 were sampled weeks to months after the bloom development (Fig. 6). The moderate to relatively high $^{234}$Th fluxes are thus surprising. Lemaitre et al., (2018) argue that the greater fluxes there might be related to the proximity of the Iberian margin, where particle dynamics were intense and lithogenic particles were numerous (Gourain et al., 2018). A temporal decoupling between production and export could be an alternative possibility. The Western European and Icelandic Basins were sampled during bloom development, and the NPP peaks occuring just before sampling may have promoted the high fluxes. In fact, these basins have been characterized by the presence of fast-sinking particles during the bloom (Villa-Alfageme et al., 2016), likely also explaining the high export. In contrast, the lower export observed in the western section may be due to the fact that the sampling occurred during the decline of the bloom, probabaly with a decoupling between production and export in the Labrador Basin, or during a particle retention event in the Irminger Basin.

Unlike the observations of higher $^{234}$Th export flux in the eastern than western sections, there were no significant differences in $^{210}$Po export flux between the two sections. This observation

supports the argument that the $^{210}$Po deficit tends to smooth out episodic events due to integration over longer time periods. The $^{210}$Po deficit records seasonal changes in export fluxes, whereas the $^{234}$Th deficit represents more recent changes in the water column (Verdeny et al., 2009; Hayes et al., 2018). Indeed, the $^{210}$Po deficit integrates the flux over months that include a period of lower flux prior to the bloom along the GA01 transect, whereas the $^{234}$Th deficit integrates the flux only over weeks that include the bloom itself at most of the stations (Fig. 6). Therefore, the specific stage of the bloom shortly prior to the sampling date appears to have less influence on the $^{210}$Po-derived than the $^{234}$Th-derived export flux along this transect.

#### 4.5.2. POC/$^{210}$Po vs. POC/$^{234}$Th ratio

In order to calculate POC export flux, one needs both the export of the daughter nuclide at a defined depth as well as the particulate POC/radionuclide ratio on the sinking particles. In situ pump filtered particles, either operationally defined as small (1-53 µm, SSF), large (> 53 µm, LSF), or total (> 1 µm, TPF) particles, may all represent a combination of sinking and non-sinking particles. In the present study, the particulate POC/radionuclide ratio on the TPF and LSF were examined and used to calculate POC export flux. The POC/$^{210}$Po and POC/$^{234}$Th ratios in the particles at the depths of ThEq were derived from the power law functions in each basin (POC/$^{210}$Po in Table 2, POC/$^{234}$Th in Lemaitre et al., (2018)). The TPF POC/$^{210}$Po and TPF POC/$^{234}$Th ratios had very similar spatial trends ($n = 11$, $R^2 = 0.8$, p-value $< 0.0001$) along the transect, with the lowest POC/radionuclide ratios in the Iberian and Western European Basins and the highest ratios in the Labrador Sea. In contrast, the LSF POC/$^{210}$Po ratios were not correlated with LSF POC/$^{234}$Th ratios ($n = 11$, $R^2 = 0.3$, p-value =0.07). The correlation of values within the TPF but not the LSF suggests that the composition of large particles was different from that of the total particles, and that the difference in particle association between POC and $^{210}$Po and $^{234}$Th was greater in large than total particles.

#### 4.5.3. $^{210}$Po-derived POC vs. $^{234}$Th-derived POC

When the radionuclide fluxes were multiplied by the POC/radionuclide values, the range of the calculated POC fluxes were negligible to 7 mmol C m$^{-2}$ d$^{-1}$ and negligible to 12 mmol C m$^{-2}$ d$^{-1}$ via the $^{210}$Po method using the TPF and LSF POC/$^{210}$Po ratios, respectively; and from 2.5 to 13 mmol C m$^{-2}$ d$^{-1}$ and from 1 to 12 mmol C m$^{-2}$ d$^{-1}$ via the $^{234}$Th method using the TPF and LSF

POC/$^{234}$Th ratios, respectively (Fig. 10). The $^{234}$Th-POC and $^{210}$Po-POC fluxes agreed within a factor of 3 along the transect, with higher POC estimates derived from the $^{234}$Th method in 9 out of 11 stations. This was consistent with previous studies that have typically found higher estimated POC flux via the $^{234}$Th method (e.g. Shimmield et al., 1995; Stewart et al., 2007; Verdeny et al., 2009).

When using the total particle POC/radionuclide ratios, only stations 26 and 60 were characterized by slightly higher $^{210}$Po-derived POC flux estimates than $^{234}$Th-derived estimates (0.2 and 1.5-fold, respectively). In contrast, at station 1 the difference between the methods was greatest, with the $^{210}$Po-derived POC flux negligible and the $^{234}$Th-POC flux of about 7 mmol C m$^{-2}$ d$^{-1}$. At stations 13, 21, and 44, the $^{234}$Th-POC fluxes were greater than $^{210}$Po-POC estimates by almost 1-fold. Whereas in the Iceland and Labrador Basins, the $^{234}$Th-POC fluxes were larger than $^{210}$Po-POC estimates by 3- and 2-fold, respectively. When using the large particle POC/radionuclide ratios, only in the Irminger Basin was there higher $^{210}$Po-derived POC flux than $^{234}$Th-derived POC flux (> 0.2 to 3-fold). In the Iberian Basin, the greatest difference between the methods was found at station 1 where $^{210}$Po-derived POC flux was negligible while $^{234}$Th-derived POC flux was the highest along the transect but with a large uncertainty (12 ± 22 mmol C m$^{-2}$ d$^{-1}$), and at station 13 the $^{234}$Th-POC flux was greater than the $^{210}$Po-POC estimate by 4-fold. In the Western European, Iceland, and Labrador Basins, the $^{234}$Th-POC fluxes were larger than $^{210}$Po-POC estimates by 5, 4, and 2-fold, respectively.

Wilcoxon rank sum tests revealed that the $^{234}$Th-POC estimates were significantly greater than $^{210}$Po-derived POC export at the stations from the Iberian Basin to the Iceland Basin ($n = 6$, TPF: p-value < 0.01, LSF: p-value < 0.02), but not at the stations from the Irminger Basin to the Labrador Basin ($n = 5$, TPF: p-value > 0.1, LSF: p-value = 1). Since the ratios of POC to radionuclides on total particles had very similar spatial trends along the transect, the discrepancy between TPF $^{234}$Th-POC and TPF $^{210}$Po-POC flux estimates must be driven primarily by the discrepancy between the SS estimates of $^{234}$Th and $^{210}$Po fluxes, discussed in section 4.5.1. In contrast, the discrepancy between the POC to isotope ratios in the large particle may have led to some degree of discrepancy between the LSF $^{234}$Th-POC and LSF $^{210}$Po-POC flux estimates.

## 5. Conclusions

This study used the water column $^{210}$Po and $^{210}$Pb activity data to constrain the $^{210}$Po particulate flux from the mixed layer depth, the base of the euphotic zone and primary production zone, and the $^{234}$Th-$^{238}$U equilibrium depth. The ratios of POC concentration to $^{210}$Po activity on the total particulate (> 1 μm) fraction and large particulate fraction (> 53 μm) were used to estimate POC export fluxes. We have been able to include vertical advection into a steady-state model to calculate the $^{210}$Po flux along the transect. The scale of $^{210}$Po fluxes due to vertical advection were of the same magnitude as the steady state fluxes calculated from the $^{210}$Po deficit alone. The $^{210}$Po-derived POC export fluxes varied spatially, ranging from negligible to 10 mmol C $m^{-2}$ $d^{-1}$ along the transect, with the highest export fluxes in the Labrador Sea. POC export efficiencies (flux relative to production) also showed regional differences, ranging from negligible to 13% along the transect. Higher export efficiencies were seen in the basins where diatoms dominated the phytoplankton community. The low export efficiencies recorded in the Iberian Basin, on the other hand, may be associated with the dominance of smaller phytoplankton, such as coccolithophores. POC export fluxes estimated from the water column $^{210}$Po/$^{210}$Pb and $^{234}$Th/$^{238}$U disequilibria agreed within a factor of 3 across our study region, with higher POC estimates generally derived from the $^{234}$Th method. The differences were attributed to integration timescales and the history of bloom events.

**Acknowledgements**

We thank the captain (Gilles Ferrand) and crew of the *R/V Pourquoi Pas?* and the chief scientists (Geráldine Sarthou and Pascale Lherminier) of the GEOVIDE cruise. We also thank Pierre Branellec, Floriane Desprez de Gésincourt, Michel Hamon, Catherine Kermabon, Philippe Le Bot, Stéphane Leizour, Olivier Ménage, Fabien Pérault, and Emmanuel de Saint-Léger for their technical support during the GEOVIDE expedition, Catherine Schmechtig for the GEOVIDE database management, and Phoebe Lam for providing two modified McLane in-situ pumps, Frédéric Planchon, Virginie Sanial, and Catherine Jeandel for their assistance with pump deployments and particulate sample collection. The authors also thank Arnout Roukaerts, Debany Fonseca-Batista, Florian Deman, and Frank Dehairs for providing primary production data. Funding for the GEOVIDE cruise was provided by the French National Research Agency (ANR-13-BS06-0014, ANR-12-PDOC-0025-01), the French National Center for Scientific Research (CNRS-LEFE-CYBER), the LabexMER (anr-10-LABX-19), and Ifremer. Gillian

Stewart and Yi Tang were supported by NSF award #OCE 1237108. The Generalitat de Catalunya also helped through its grant 2017 SGR-1588. This work is contributing to the ICTA 'Unit of Excellence' (MinECo, MDM2015-0552). Maxi Castrillejo and Montserrat Roca-Marti were funded by an FPU PhD studentship (AP-2012-2901 and AP2010-2510, respectively) from the Ministerio de Educación, Cultura y Deporte of Spain. Maxi Castrillejo was also supported by the ETH Zurich Postdoctoral Fellowship Program (17-2 FEL-30), co-funded by the Marie Curie Actions for People COFUND Program. We also thank Gary Hemming (Queens College) and Troy Rasbury (Stony Brook University) for laboratory assistance with the ICP-MS analyses. Finally, we thank the Associate Editore and the anonymous reviewers for their helpful comments on how to improve the manuscript.

## References


Acker, J. G. and Leptoukh, G.: Online Analysis Enhances Use of NASA Earth Science Data, Eos, Trans. AGU, 88, 14-17, 2007.

Bhat, S. G., Krishnaswamy, S., Lal, D., Rama and Moore, W. S.: 234Th/238U ratios in the ocean, Earth and Planetary Science Letters, 5 IS -, 483-491, 1968.

Buesseler, K. O.: The decoupling of production and particulate export in the surface ocean, Global Biogeochemcal Cycles, 12, 297-310, 10.1029/97GB03366, 1998.

Buesseler, K. O., Bacon, M. P., Kirk Cochran, J. and Livingston, H. D.: Carbon and nitrogen export during the JGOFS North Atlantic Bloom experiment estimated from 234Th:238U disequilibria, Deep Sea Research Part A. Oceanographic Research Papers, 39, 1115-1137, 1992.

Cherrier, J., Burnett, W. C. and LaRock, P. A.: Uptake of polonium and sulfur by bacteria, Geomicrobiology Journal, 13, 103-115, 10.1080/01490459509378009, 1995.

Chuang, C., Santschi, P. H., Ho, Y., Conte, M. H., Guo, L., Schumann, D., Ayranov, M. and Li, Y.: Role of biopolymers as major carrier phases of Th, Pa, Pb, Po, and Be radionuclides in settling particles from the Atlantic Ocean, Marine Chemistry, 157, 131-143, 2013.

Cochran, J. K.: Uranium-Series Disequilibrium - Application to Earth, Marine, and Environmental Sciences, The oceanic chemistry of the uranium and thorium-series nuclides. Oxford University Press, 334-395, 1992.

Djogic, R., Sipos, L. and Branica, M.: Characterization of uranium(VI) in seawater, Limnology and Oceanography, 31, 1122-1131, 10.4319/lo.1986.31.5.1122, 1986.

Ducklow, H., Steinberg, D. and Buesseler, K.: Upper Ocean Carbon Export and the Biological Pump, Oceanography, 14, 50-58, 10.5670/oceanog.2001.06, 2001.

Durkin, C. A., Van Mooy, B. A. S., Dyhrman, S. T. and Buesseler, K. O.: Sinking phytoplankton associated with carbon flux in the Atlantic Ocean, Limnology and Oceanography, 61, 1172-1187, 10.1002/lno.10253, 2016.

Falkowski, P. G., Barber, R. T. and Smetacek, V.: Biogeochemical Controls and Feedbacks on Ocean Primary Production, Science, 281, 200-206, 1998.

Fisher, N. S., Burns, K. A., Cherry, R. D. and Heyraud, M.: Accumulation and cellular distribution of 241Am, 210Po and 210Pb in two marine algae, Marine Ecology Progress Series, 11, 233-237, 1983.

Fleer, A. P. and Bacon, M. P.: Determination of 210Pb and 210Po in seawater and marine particulate matter, Nuclear Instruments and Methods in Physics Research, 223, 243-249, 1984.

Flynn, W. W.: The determination of low levels of polonium-210 in environmental materials, Analytica Chimica Acta, 43, 221-227, 1968.

Fonseca-Batista, D., Li, X., Riou, V., Michotey, V., Fripiat, F., Deman, F., Guasco, S., Brion, N., Lemaitre, N., Planchon, F., Tonnard, M., Planquette, H., Gallinari, M., Sarthou, G., Elskens, M., Chou, L. and Dehairs, F.: Evidence of high N2 fixation rates in productive waters of the temperate Northeast Atlantic, Biogeosciences, 2018.

Friedrich, J. and Rutgers van der Loeff, M. M.: A two-tracer (210Po–234Th) approach to distinguish organic carbon and biogenic silica export flux in the Antarctic Circumpolar Current, Deep Sea Research Part I: Oceanographic Research Papers, 49, 101-120, 10.1016/S0967-0637(01)00045-0, 2002.

García-Ibáñez, M. I., Pérez, F. F., Lherminier, P., Zunino, P., Mercier, H. and Tréguer, P.: Water mass distributions and transports for the 2014 GEOVIDE cruise in the North Atlantic, Biogeosciences, 15, 2075-2090, https://doi.org/10.5194/bg-15-2075-2018, 2018.

Gourain, A., Planquette, H., Cheize, M., Menzel-Barraqueta, J. L., Boutorh, J., Shelley, R. U., Pereira-Contreira, L., Lemaitre, N., Lacan, F., Lherminier, P. and Sarthou, G.: Particualte trace metals along the GEOVIDE section, Biogeosciences, 2018.

Guidi, L., Stemmann, L., Legendre, L., Picheral, M., Prieur, L. and Gorsky, G.: Vertical distribution of aggregates (>110 µm) and mesoscale activity in the northeastern Atlantic: Effects on the deep vertical export of surface carbon, Limnology and Oceanography, 52, 7-18, doi:10.4319/lo.2007.52.1.0007, 2007.

Hayes, C. T., Black, E. E., Andersen, R. A., Baskaran, M., Buesseler, K. O., Charette, M. A., Cheng, H., Cochran, J. K., Edwards, R. L., Fitzgerald, P., Lam, P. J., Lu, Y., Morris, S. O., Ohnemus, D. C., Pavia, F. J., Stewart, G. and Tang, Y.: Flux of particulate elements in the North Atlantic Ocean constrained by multiple radionuclides, Global Biogeochemcal Cycles, https://doi.org/10.1029/2018GB005994, 2018

Honjo, S., Manganini, S. J., Krishfield, R. A. and Francois, R.: Particulate organic carbon fluxes to the ocean interior and factors controlling the biological pump: A synthesis of global sediment trap programs since 1983, Progress in Oceanography, 76, 217-285, 2008.

Jerlov, N. G.: Optical Oceanography. Elsevier Publishing Company, 1968.

Kemp, A. E. S., Pearce, R. B., Grigorov, I., Rance, J., Lange, C. B., Quilty, P. and Salter, I.: Production of giant marine diatoms and their export at oceanic frontal zones: Implications for Si

and C flux from stratified oceans, Global Biogeochemical Cycles, 20, doi:10.1029/2006GB002698, 2006.

Kim, G. and Church, T. M.: Seasonal biogeochemical fluxes of 234Th and 210Po in the Upper Sargasso Sea: Influence from atmospheric iron deposition, Global Biogeochemcal Cycles, 15, 651-661, 10.1029/2000GB001313, 2001.

Lemaitre, N., Planchon, F., Planquette, H., Dehairs, F., Batista, D. F., Roukaerts, A., Deman, F., Tang, Y., Mariez, C. and Sarthou, G.: High variability of export fluxes along the North Atlantic GEOTRACES section GA01: Particulate organic carbon export deduced from the 234Th method, Biogeosciences, 15, 6417-6437, https://doi.org/10.5194/bg-15-6417-2018, 2018.

Lévy, M., Iovino, D., Resplandy, L., Klein, P., Madec, G., Tréguier, A. M., Masson, S. and Takahashi, K.: Large-scale impacts of submesoscale dynamics on phytoplankton: Local and remote effects, Ocean Modelling, 43-44, 77-93, https://doi.org/10.1016/j.ocemod.2011.12.003, 2012.

Masqué, P., Sanchez-Cabeza, J. A., Bruach, J. M., Palacios, E. and Canals, M.: Balance and residence times of 210Pb and 210Po in surface waters of the northwestern Mediterranean Sea, Continental Shelf Research, 22, 2127-2146, 10.1016/S0278-4343(02)00074-2, 2002.

Menemenlis, D., Campin, J., Heimbach, P., Hill, C., Lee, T., Nguyen, A., Schodlock, M. and Zhang, H.: ECCO2: High Resolution Global Ocean and Sea Ice Data Synthesis, Mercator Ocean Quarterly Newsletter, 31, 13-21, 2008.

Moore, H. E., Poet, S. E., Martell, E. A. and Wilkening, M. H.: Origin of 222Rn and its long-lived daughters in air over Hawaii, Journal of Geophysical Research, 79, 5019-5024, doi:10.1029/JC079i033p05019, 1974.

Murray, J. W., Paul, B., Dunne, J. P. and Chapin, T.: 234Th, 210Pb, 210Po and stable Pb in the central equatorial Pacific: Tracers for particle cycling, Deep Sea Research Part I: Oceanographic Research Papers, 52, 2109-2139, 2005.

Murray, J. W., Young, J., Newton, J., Dunne, J., Chapin, T., Paul, B. and McCarthy, J. J.: Export flux of particulate organic carbon from the central equatorial Pacific determined using a combined drifting trap-234Th approach, Deep Sea Research Part II, 43, 1095-1132, 10.1016/0967-0645(96)00036-7, 1996.

Owens, S. A., Pike, S. and Buesseler, K. O.: Thorium-234 as a tracer of particle dynamics and upper ocean export in the Atlantic Ocean, Deep Sea Research Part II, 116, 42-59, 10.1016/j.dsr2.2014.11.010, 2015.

Quigley, M. S., Santschi, P. H., Hung, C., Guo, L. and Honeyman, B. D.: Importance of acid polysaccharides for 234Th complexation to marine organic matter, Limnology and Oceanography, 47, 367-377, 10.4319/lo.2002.47.2.0367, 2002.

Richardson, T. L. and Jackson, G. A.: Small Phytoplankton and Carbon Export from the Surface Ocean, Science, 315, 838-840, 10.1126/science.1133471, 2007.

Rigaud, S., Puigcorbé, V., Camara-Mor, P., Casacuberta, N., Roca-Martí, M., Garcia-Orellana, J., Benitez-Nelson, C. R., Masqué, P. and Church, T.: A methods assessment and recommendations for improving calculations and reducing uncertainties in the determination of 210Po and 210Pb activities in seawater, Limnology and Oceanography Methods, 11, 561-571, 10.4319/lom.2013.11.561, 2013.

Rigaud, S., Stewart, G., Baskaran, M., Marsan, D. and Church, T.: 210Po and 210Pb distribution, dissolved-particulate exchange rates, and particulate export along the North Atlantic US GEOTRACES GA03 section, Deep Sea Research Part II, 116, 60-78, 10.1016/j.dsr2.2014.11.003, 2015.

Rivière, P. and Pondaven, P.: Phytoplankton size classes competitions at sub-mesoscale in a frontal oceanic region, Journal of Marine Systems, 60, 345-364, https://doi.org/10.1016/j.jmarsys.2006.02.005, 2006.

Roca-Martí, M., Puigcorbé, V., Rutgers van der Loeff, M. M., Katlein, C., Fernández-Méndez, M., Peeken, I. and Masqué, P.: Carbon export fluxes and export efficiency in the central Arctic during the record sea-ice minimum in 2012: a joint 234Th/238U and 210Po/210Pb study, Journal of Geophysical Research: Oceans, 121, 5030-5049, 10.1002/2016JC011816, 2016.

Rutgers van der Loeff, M. M., Friedrich, J. and Bathmann, U. V.: Carbon export during the Spring Bloom at the Antarctic Polar Front, determined with the natural tracer 234Th, Deep Sea Research Part II, 44, 457-478, 10.1016/S0967-0645(96)00067-7, 1997.

Sabine, C. L.: The Oceanic Sink for Anthropogenic CO2, Science, 305, 367-371, 10.1126/science.1097403, 2004.

Sarin, M. M., Kim, G. and Church, T. M.: 210Po and 210Pb in the South-equatorial Atlantic: distribution and disequilibrium in the upper 500 m, Deep Sea Research Part II, 46, 907-917, 1999.

Savoye, N., Benitez-Nelson, C., Burd, A. B., Cochran, J. K., Charette, M., Buesseler, K. O., Jackson, G. A., Roy-Barman, M., Schmidt, S. and Elskens, M.: 234Th sorption and export models in the water column: A review, Marine Chemistry, 100, 234-249, 2006.

Shelley, R. U., Roca-Martí, M., Castrillejo, M., Sanial, V., Masqué, P., Landing, W. M., van Beek, P., Planquette, H. and Sarthou, G.: Quantification of trace element atmospheric deposition

fluxes to the Atlantic Ocean (> 40°N; GEOVIDE, GEOTRACES GA01) during spring 2014, Deep Sea Research Part I: Oceanographic Research Papers, 119, 34-49, 10.1016/j.dsr.2016.11.010, 2017.

Shimmield, G. B., Ritchie, G. D. and Fileman, T. W.: The impact of marginal ice zone processes on the distribution of 210Pb, 210Po and 234Th and implications for new production in the Bellingshausen Sea, Antarctica, Deep Sea Research Part II, 42, 1313-1335, 10.1016/0967-0645(95)00071-W, 1995.

Stewart, G., Cochran, J. K., Miquel, J. C., Masqué, P., Szlosek, J., Rodriguez y Baena, A. M., Fowler, S. W., Gasser, B. and Hirschberg, D. J.: Comparing POC export from 234Th/238U and 210Po/210Pb disequilibria with estimates from sediment traps in the northwest Mediterranean, Deep Sea Research Part I: Oceanographic Research Papers, 54, 1549-1570, 10.1016/j.dsr.2007.06.005, 2007.

Stewart, G. M., Bradley Moran, S. and Lomas, M. W.: Seasonal POC fluxes at BATS estimated from 210Po deficits, Deep Sea Research Part I: Oceanographic Research Papers, 57, 113-124, 10.1016/j.dsr.2009.09.007, 2010.

Stewart, G. M. and Fisher, N. S.: Bioaccumulation of polonium-210 in marine copepods, Limnology and Oceanography, 48, 2011-2019, 10.4319/lo.2003.48.5.2011, 2003a.

Stewart, G. M. and Fisher, N. S.: Experimental studies on the accumulation of polonium-210 by marine phytoplankton, Limnology and Oceanography, 48, 1193-1201, 10.4319/lo.2003.48.3.1193, 2003b.

Subha Anand, S., Rengarajan, R., Shenoy, D., Gauns, M. and Naqvi, S. W. A.: POC export fluxes in the Arabian Sea and the Bay of Bengal: A simultaneous 234Th/238U and 210Po/210Pb study, Marine Chemistry, https://doi.org/10.1016/j.marchem.2017.11.005, 2017.

Tang, Y., Castrillejo, M., Roca-Martí, M., Masqué, P., Lemaitre, N. and Stewart, G.: Distributions of total and size-fractionated particulate 210Po and 210Pb activities along the North Atlantic GEOTRACES GA01 transect: GEOVIDE cruise, Biogeosciences, 15, 5437-5453, https://doi.org/10.5194/bg-15-5437-2018, 2018.

Tang, Y., Stewart, G., Lam, P. J., Rigaud, S. and Church, T.: The influence of particle concentration and composition on the fractionation of 210Po and 210Pb along the North Atlantic GEOTRACES transect GA03, Deep Sea Research Part I: Oceanographic Research Papers, 128, 42-54, 10.1016/j.dsr.2017.09.001, 2017.

Turekian, K. K., Nozaki, Y. and Benninger, L. K.: Geochemistry of Atmospheric Radon and Radon Products, Annual Review of Earth and Planetary Sciences, 5, 227-255, 10.1146/annurev.ea.05.050177.001303, 1977.

Verdeny, E., Masqué, P., Garcia-Orellana, J., Hanfland, C., Kirk Cochran, J. and Stewart, G. M.: POC export from ocean surface waters by means of 234Th/238U and 210Po/210Pb disequilibria: A review of the use of two radiotracer pairs, Deep Sea Research Part II, 56, 1502-1518, 10.1016/j.dsr2.2008.12.018, 2009.

Verdeny, E., Masqué, P., Maiti, K., Garcia-Orellana, J., Bruach, J. M., Mahaffey, C. and Benitez-Nelson, C. R.: Particle export within cyclonic Hawaiian lee eddies derived from 210Pb–210Po disequilibrium, Deep Sea Research Part II: Topical Studies in Oceanography, 55, 1461-1472, 10.1016/j.dsr2.2008.02.009, 2008.

Villa-Alfageme, M., Soto, F. C., Ceballos, E., Giering, S. L. C., Le Moigne, F. A. C., Henson, S., Mas, J. L. and Sanders, R. J.: Geographical, seasonal, and depth variation in sinking particle speeds in the North Atlantic, Geophysical Research Letters, 43, 8609-8616, doi:10.1002/2016GL069233, 2016.

Waite, A. M., Stemmann, L., Guidi, L., Calil, P. H. R., Hogg, A. M. C., Feng, M., Thompson, P. A., Picheral, M. and Gorsky, G.: The wineglass effect shapes particle export to the deep ocean in mesoscale eddies, Geophysical Research Letters, 43, 9791-9800, doi:10.1002/2015GL066463, 2016.

Wei, C. L., Lin, S. Y., Sheu, D. D. D., Chou, W. C., Yi, M. C., Santschi, P. H. and Wen, L. S.: Particle-reactive radionuclides 234Th, 210Pb, 210Po as tracers for the estimation of export production in the South China Sea, Biogeosciences, 8, 3793-3808, 2011.

Wei, C. L., Yi, M. C., Lin, S. Y., Wen, L. S. and Lee, W. H.: Seasonal distributions and fluxes of 210Pb and 210Po in the northern South China Sea, Biogeosciences, 11, 6813-6826, 2014.

Weller, R. A. and Plueddemann, A. J.: Observations of the vertical structure of the oceanic boundary layer, Journal of Geophysical Research: Oceans, 101, 8789-8806, 10.1029/96JC00206, 1996.

Yang, W., Guo, L., Chuang, C., Schumann, D., Ayranov, M. and Santschi, P. H.: Adsorption characteristics of 210Pb, 210Po and 7Be onto micro-particle surfaces and the effects of macromolecular organic compounds, Geochimica et Cosmochimic Acta, 107 47-64, 2013.

Zunino, P., Lherminier, P., Mercier, H., Daniault, N., Garcia-Ibanez, M. I. and Pérez, F. F.: The GEOVIDE cruise in May-June 2014 revealed an intense MOC over a cold and fresh subpolar North Atlantic, Biogeosciences, 2018.

Table 1. The mixed layer depth (MLD, defined as a change in potential density of 0.03 kg $m^{-3}$ relative to the potential density at 10 m), the depth of the euphotic zone ($Z_{1\%}$, defined as the depth where photosynthetic available radiation was 1% of its surface value), the primary production zone (PPZ, at which the fluorescence reaches 10% of its maximum), and the $^{234}$Th-$^{238}$U equilibrium depth (ThEq) at each station along the GA01 transect. Together with the 30-day (30 days prior to the sampling date) average vertical velocity within the 20 m under the corresponding depths ($w_{20}$, $10^{-6}$ m $s^{-1}$, downwards as positive direction). Primary production (PP) and net primary production (NPP) rates derived from 24-hour bottle incubations (Fonseca-Batista et al., 2018; Lemaitre et al., 2018) and from the VGPM products, respectively, are also presented. Note the NPP rates were averaged for the previous 138 days ($^{210}$Po half-life) prior to the sampling date.

| St. | Sampling date | Basin | Integration Depth (m) | | | | $w_{20}$ ($10^{-6}$ m $s^{-1}$) | | | | Production (mmol C $m^{-2}$ $d^{-1}$) | | | |
|---|---|---|---|---|---|---|---|---|---|---|---|---|---|---|
| | | | MLD | $Z_{1\%}$ | PPZ | ThEq | MLD | $Z_{1\%}$ | PPZ | ThEq | PP | ± | NPP | ± |
| 1 | 5/19/14 | Iberian Basin | 15 | 40 | 136 | 90 | -1±5 | -1±4 | -3±2 | -2±6 | 33 | 2 | 69 | 43 |
| 13 | 5/24/14 | Iberian Basin | 35 | 40 | 90 | 110 | 0.1±3.1 | 0.1±3.1 | -2±5 | 0.4±54.6 | 79 | 3 | 61 | 32 |
| 21 | 5/31/14 | Western European Basin | 15 | 32 | 64 | 110 | -1±2 | -1±4 | -1±5 | 0.1±5 | 135 | 2 | 109 | 112 |
| 26 | 6/4/14 | Western European Basin | 30 | 30 | 98 | 100 | -2±3 | -2±2 | -5±5 | -5±4 | 174 | 19 | 58 | 57 |
| 32 | 6/7/14 | Iceland Basin | 30 | 31 | 70 | 120 | -1±9 | -1±9 | -4±20 | -3±20 | 105 | 11 | 48 | 36 |
| 38 | 6/10/14 | Iceland Basin | 30 | 30 | 69 | 80 | 1±3 | 1±3 | 3±4 | 3±5 | 68 | 7 | 44 | 37 |
| 44 | 6/13/14 | Irminger Basin | 26 | 22 | 44 | 40 | 1±2 | 1±2 | 2±3 | 2±3 | 137 | 2 | 46 | 44 |
| 60 | 6/18/18 | Irminger Basin | 17 | 20 | 36 | 100 | -14±20 | -14±20 | -36±40 | -11±70 | 166 | 32 | 50 | 51 |
| 64 | 6/19/14 | Labrador Basin | 20 | 47 | 80 | 80 | 2±6 | 7±7 | 3±7 | 3±7 | 54 | 18 | 47 | 49 |
| 69 | 6/22/14 | Labrador Basin | 20 | 28 | 44 | 40 | -2±1 | -2±3 | -2±3 | -2±3 | 27 | 5 | 46 | 56 |
| 77 | 6/26/14 | Labrador Basin | 15 | 20 | 59 | 80 | 4±5 | 4±7 | 7±10 | 9±20 | 80 | 21 | 50 | 56 |

Table 2. The total $^{210}$Po flux as the sum of the flux calculated from the deficit and vertical advection, together with POC/$^{210}$Po ratios in particles > 1 μm (derived from the power law function in Fig. 5) and POC fluxes derived from $^{210}$Po at the corresponding depths. The uncertainties of $^{210}$Po export flux are associated with the activity uncertainty of the radionuclides. The error for the calculated particulate POC/$^{210}$Po ratio in each basin is the standard error of regression. The uncertainties of the $^{210}$Po-derived POC flux were estimated based on the propagation of error. (Editors/Reviewers please NB: This is a table with 53 columns that has been divided into 3 pieces for review purposes, but which should be published as one long table.)

| St. | Integration Depth (m) | | | | $^{210}$Po flux (dpm m$^{-2}$ d$^{-1}$): $^{210}$Po/$^{210}$Pb term | | | | | | | | $^{210}$Po flux (dpm m$^{-2}$ d$^{-1}$): vertical advection term | | | | | | | |
|---|---|---|---|---|---|---|---|---|---|---|---|---|---|---|---|---|---|---|---|---|
| | MLD | $Z_{1\%}$ | PPZ | ThEq | MLD | ± | $Z_{1\%}$ | ± | PPZ | ± | ThEq | ± | MLD | ± | $Z_{1\%}$ | ± | PPZ | ± | ThEq | ± |
| 1 | 15 | 40 | 136[a] | 90[a] | 1.1 | 0.3 | 1.5 | 0.8 | -4.5 | 2.2 | -0.9 | 1.6 | 2.4 | 19.7 | 3.6 | 14.7 | 6.8 | 4.8 | 4.6 | 16.2 |
| 13 | 35[a] | 40 | 90[a] | 110[a] | 3.4 | 0.9 | 4.1 | 0.9 | 4.3 | 1.8 | 3.7 | 2.0 | -0.2 | 5.2 | -0.2 | 5.6 | 3.7 | 10.0 | 1.0 | 10.6 |
| 21 | 15 | 32[a] | 64[a] | 110[a] | -0.6 | 0.5 | -0.7 | 0.8 | 2.2 | 1.2 | 3.5 | 1.8 | -1.1 | 4.0 | -0.4 | 1.7 | 2.7 | 9.9 | 0.01 | 0.40 |
| 26 | 30 | 30 | 98[a] | 100 | 4.8 | 1.5 | 4.8 | 1.5 | 15.2 | 3.1 | 26.4 | 4.8 | -0.9 | 3.2 | -0.9 | 3.2 | 4.0 | 4.0 | 2.8 | 4.0 |
| 32 | 30 | 31[a] | 70[a] | 120[a] | 4.7 | 0.9 | 4.8 | 0.9 | 9.1 | 1.4 | 8.5 | 2.2 | -1.6 | 12.2 | -1.6 | 12.0 | 7.9 | 33.4 | 3.0 | 23.3 |
| 38 | 30 | 30 | 69[a] | 80 | -0.5 | 1.3 | -0.5 | 1.3 | 3.7 | 2.5 | 5.2 | 2.6 | 0.4 | 1.8 | 0.4 | 1.8 | -1.0 | 3.5 | -0.9 | 4.9 |
| 44 | 26[a] | 22[a] | 44[a] | 40 | 1.5 | 1.0 | 1.0 | 1.0 | 4.2 | 1.4 | 3.6 | 1.4 | 0.9 | 2.1 | 1.1 | 2.5 | 0.9 | 2.2 | 1.5 | 2.8 |
| 60 | 17[a] | 20 | 36[a] | 100 | 3.1 | 1.1 | 3.8 | 1.1 | 9.8 | 1.6 | 37 | 5.4 | -24.9 | 49.6 | -40.4 | 74.9 | -36.2 | 69.0 | 14.1 | 87.1 |
| 64 | 20[a] | 47[a] | 80 | 80 | 5.8 | 0.8 | 9.8 | 2.1 | 17.8 | 3.2 | 18 | 3.2 | -0.7 | 2.9 | -4.3 | 8.8 | -0.5 | 3.7 | -0.5 | 3.7 |
| 69 | 20[a] | 28[a] | 44[a] | 40 | 4.0 | 0.7 | 6.1 | 0.8 | 8.5 | 1.6 | 8.3 | 1.5 | 1.9 | 3.3 | 3.4 | 5.8 | 5.8 | 7.9 | 6.7 | 8.9 |
| 77 | 15[a] | 20 | 59[a] | 80 | 2.2 | 0.6 | 2.9 | 0.7 | 7.0 | 2.4 | 9.8 | 2.9 | -0.6 | 5.2 | 0.3 | 6.4 | 3.0 | 9.9 | -15 | 29 |

[a]For the depths at which total radionuclides data are not available, the measured values of total $^{210}$Po and $^{210}$Pb activities were linearly interpolated at the missing depths.

Table 2. (continued)

| St. | $^{210}$Po flux (dpm m$^{-2}$ d$^{-1}$): total flux | | | | | | | | POC/$^{210}$Po ($\mu$mol dpm$^{-1}$) | | | | | | | |
|---|---|---|---|---|---|---|---|---|---|---|---|---|---|---|---|---|
| | MLD | ± | $Z_{1\%}$ | ± | PPZ | ± | ThEq | ± | MLD | ± | $Z_{1\%}$ | ± | PPZ | ± | ThEq | ± |
| 1 | 3.5 | 19.7 | 5.1 | 14.7 | 2.3 | 5.3 | 3.6 | 16.2 | 540 | 67 | 305 | 67 | 150 | 67 | 190 | 67 |
| 13 | 3.2 | 5.3 | 3.9 | 5.7 | 7.9 | 10.1 | 4.7 | 10.8 | 330 | 67 | 305 | 67 | 190 | 67 | 169 | 67 |
| 21 | -1.7 | 4.1 | -1.1 | 1.8 | 4.9 | 10.0 | 3.5 | 1.9 | 542 | 89 | 389 | 89 | 287 | 89 | 227 | 89 |
| 26 | 3.9 | 3.5 | 3.9 | 3.5 | 17.7 | 5.1 | 29.2 | 6.2 | 400 | 89 | 400 | 89 | 238 | 89 | 236 | 89 |
| 32 | 3.0 | 12.2 | 3.2 | 12.1 | 17.0 | 33.4 | 11.6 | 23.4 | 367 | 111 | 363 | 111 | 265 | 111 | 216 | 111 |
| 38 | -0.2 | 2.3 | -0.2 | 2.3 | 2.7 | 4.3 | 4.2 | 5.6 | 367 | 111 | 367 | 111 | 267 | 111 | 252 | 111 |
| 44 | 2.5 | 2.3 | 2.1 | 2.7 | 5.1 | 2.6 | 5.1 | 3.1 | 310 | 107 | 330 | 107 | 254 | 107 | 263 | 107 |
| 60 | -21.8 | 49.6 | -36.6 | 74.5 | -26.4 | 69.0 | 51.2 | 87.2 | 364 | 107 | 342 | 107 | 274 | 107 | 187 | 107 |
| 64 | 5.1 | 3.0 | 5.5 | 9.0 | 17.4 | 4.9 | 17.4 | 4.9 | 675 | 152 | 375 | 152 | 261 | 152 | 261 | 152 |
| 69 | 5.9 | 3.4 | 9.4 | 5.8 | 14.4 | 8.0 | 15.0 | 9.0 | 675 | 152 | 536 | 152 | 393 | 152 | 419 | 152 |
| 77 | 1.5 | 5.2 | 3.1 | 6.4 | 10.1 | 10 | -4.8 | 29.0 | 822 | 152 | 675 | 152 | 321 | 152 | 261 | 152 |

Table 2. (continued)

| St. | $^{210}$Po-POC flux (mmol C m$^{-2}$ d$^{-1}$): $^{210}$Po/$^{210}$Pb term | | | | | | | | $^{210}$Po-POC flux (mmol C m$^{-2}$ d$^{-1}$): total flux | | | | | | | |
|---|---|---|---|---|---|---|---|---|---|---|---|---|---|---|---|---|
| | MLD | ± | $Z_{1\%}$ | ± | PPZ | ± | ThEq | ± | MLD | ± | $Z_{1\%}$ | ± | PPZ | ± | ThEq | ± |
| 1 | 0.6 | 0.2 | 0.4 | 0.3 | -0.7 | 0.4 | -0.2 | 0.3 | 1.9 | 10.7 | 1.5 | 4.5 | 0.3 | 0.8 | 0.7 | 3.1 |
| 13 | 1.1 | 0.4 | 1.3 | 0.4 | 0.8 | 0.4 | 0.6 | 0.4 | 1.0 | 1.8 | 1.2 | 1.7 | 1.5 | 2.0 | 0.8 | 1.9 |
| 21 | -0.3 | 0.3 | -0.3 | 0.3 | 0.6 | 0.4 | 0.8 | 0.5 | -0.9 | 2.2 | -0.4 | 0.7 | 1.4 | 2.9 | 0.8 | 0.5 |
| 26 | 1.9 | 0.7 | 1.9 | 0.7 | 3.6 | 1.5 | 6.2 | 2.6 | 1.5 | 1.4 | 1.5 | 1.4 | 4.6 | 2.0 | 6.9 | 3.0 |
| 32 | 1.7 | 0.6 | 1.7 | 0.6 | 2.4 | 1.1 | 1.8 | 1.1 | 1.1 | 4.5 | 1.1 | 4.4 | 4.5 | 9.1 | 2.5 | 5.2 |
| 38 | -0.2 | 0.5 | -0.2 | 0.5 | 1.0 | 0.8 | 1.3 | 0.9 | -0.1 | 0.8 | -0.1 | 0.8 | 0.7 | 1.2 | 1.1 | 1.5 |
| 44 | 0.5 | 0.4 | 0.3 | 0.4 | 1.1 | 0.6 | 1.0 | 0.5 | 0.8 | 0.8 | 0.7 | 0.9 | 1.3 | 0.9 | 1.4 | 1.0 |
| 60 | 1.1 | 0.5 | 1.3 | 0.5 | 2.7 | 1.1 | 6.9 | 4.1 | -7.9 | 20 | -12.5 | 25.9 | -7.2 | 19.1 | 9.6 | 17.2 |
| 64 | 3.9 | 1.0 | 3.7 | 1.7 | 4.7 | 2.8 | 4.7 | 2.8 | 3.5 | 2.1 | 2.1 | 3.5 | 4.5 | 2.9 | 4.5 | 2.9 |
| 69 | 2.7 | 0.8 | 3.3 | 1.0 | 3.4 | 1.4 | 3.5 | 1.4 | 4.0 | 2.5 | 5.1 | 3.4 | 5.7 | 3.8 | 6.3 | 4.4 |
| 77 | 1.8 | 0.6 | 1.9 | 0.6 | 2.3 | 1.3 | 2.5 | 1.7 | 1.3 | 4.3 | 2.1 | 4.3 | 3.2 | 3.6 | -1.3 | 7.6 |

Table 3. The ratio of POC concentration to $^{210}Po$ activity (POC/$^{210}Po$) in the particles collected by in situ pumps. SSF: small size fraction (1-53 μm); LSF: large size fraction (> 53 μm); TPF: total ~~s~~particulate fraction (> 1 μm).

| Station | Depth (m) | POC/$^{210}Po$ (μmol dpm$^{-1}$) | | | | | |
|---|---|---|---|---|---|---|---|
| | | SSF | ± | LSF | ± | ~~TSF~~TPF | ± |
| 1 | 30 | 276 | 32 | 414 | 58 | 296 | 30 |
| 1 | 80 | 166 | 28 | 1040 | 159 | 355 | 44 |
| 1 | 550 | 41 | 4 | 31 | 4 | 39 | 4 |
| 1 | 800 | 18 | 17 | 19 | 4 | 19 | 10 |
| 1 | 120 | 108 | 14 | 222 | 42 | 117 | 13 |
| 1 | 250 | 65 | 7 | 63 | 9 | 65 | 6 |
| 13 | 60 | 289 | 29 | 216 | 26 | 281 | 25 |
| 13 | 100 | 206 | 20 | 132 | 14 | 198 | 17 |
| 13 | 200 | 79 | 7 | 50 | 8 | 76 | 7 |
| 13 | 450 | 73 | 7 | 35 | 7 | 69 | 6 |
| 21 | 80 | 622 | 51 | 13405 | 2599 | 1280 | 96 |
| 21 | 120 | 133 | 18 | 2398 | 407 | 380 | 44 |
| 21 | 250 | 85 | 9 | 482 | 133 | 109 | 10 |
| 21 | 450 | 54 | 6 | 117 | 14 | 60 | 6 |
| 26 | 30 | 377 | 70 | 310 | 34 | 350 | 42 |
| 26 | 83 | 271 | 41 | 289 | 37 | 280 | 28 |
| 26 | 153 | 275 | 94 | 118 | 14 | 209 | 43 |
| 26 | 403 | 67 | 21 | 43 | 19 | 62 | 17 |
| 32 | 30 | 492 | 60 | 733 | 382 | 500 | 59 |
| 32 | 60 | 379 | 43 | 337 | 87 | 376 | 40 |
| 32 | 100 | 311 | 39 | 376 | 56 | 326 | 33 |
| 32 | 200 | 145 | 17 | 133 | 30 | 144 | 15 |
| 32 | 450 | 41 | 5 | 55 | 9 | 42 | 4 |
| 32 | 800 | 25 | 4 | 55 | 7 | 29 | 4 |
| 38 | 20 | 254 | 38 | 345 | 108 | 258 | 37 |
| 38 | 60 | 339 | 51 | 284 | 66 | 333 | 46 |
| 38 | 109 | 157 | 15 | 196 | 23 | 163 | 13 |
| 44 | 20 | 1025 | 115 | 3085 | 798 | 1176 | 124 |
| 44 | 40 | 463 | 58 | 1379 | 1787 | 475 | 59 |
| 44 | 80 | 140 | 14 | 90 | 23 | 137 | 13 |
| 44 | 150 | 102 | 18 | 97 | 56 | 102 | 17 |
| 44 | 300 | 47 | 7 | 25 | 7 | 45 | 6 |
| 60 | 8 | 306 | 30 | 1003 | 150 | 422 | 36 |

| | | | | | | | |
|---|---|---|---|---|---|---|---|
| 60 | 60 | 232 | 33 | 851 | 193 | 272 | 36 |
| 60 | 100 | 197 | 33 | 303 | 72 | 209 | 31 |
| 60 | 250 | 61 | 7 | 294 | 84 | 72 | 8 |
| 64 | 30 | 525 | 77 | 656 | 83 | 580 | 58 |
| 64 | 60 | 455 | 75 | 286 | 77 | 434 | 64 |
| 64 | 100 | 439 | 49 | 319 | 44 | 420 | 41 |
| 64 | 150 | 107 | 36 | 158 | 28 | 129 | 24 |
| 64 | 400 | 40 | 5 | 48 | 8 | 41 | 4 |
| 69 | 20 | 347 | 44 | 879 | 164 | 397 | 46 |
| 69 | 60 | 78 | 6 | 657 | 216 | 84 | 7 |
| 69 | 100 | 257 | 26 | 359 | 44 | 268 | 24 |
| 69 | 150 | 125 | 14 | 127 | 25 | 125 | 13 |
| 69 | 410 | 30 | 3 | 71 | 8 | 34 | 3 |
| 77 | 10 | 1281 | 309 | 917 | 150 | 1181 | 213 |
| 77 | 50 | 1372 | 357 | 1020 | 412 | 1339 | 320 |
| 77 | 80 | 512 | 63 | 544 | 103 | 516 | 57 |
| 77 | 200 | 84 | 13 | 217 | 79 | 92 | 13 |
| 77 | 460 | 22 | 3 | 59 | 6 | 27 | 3 |

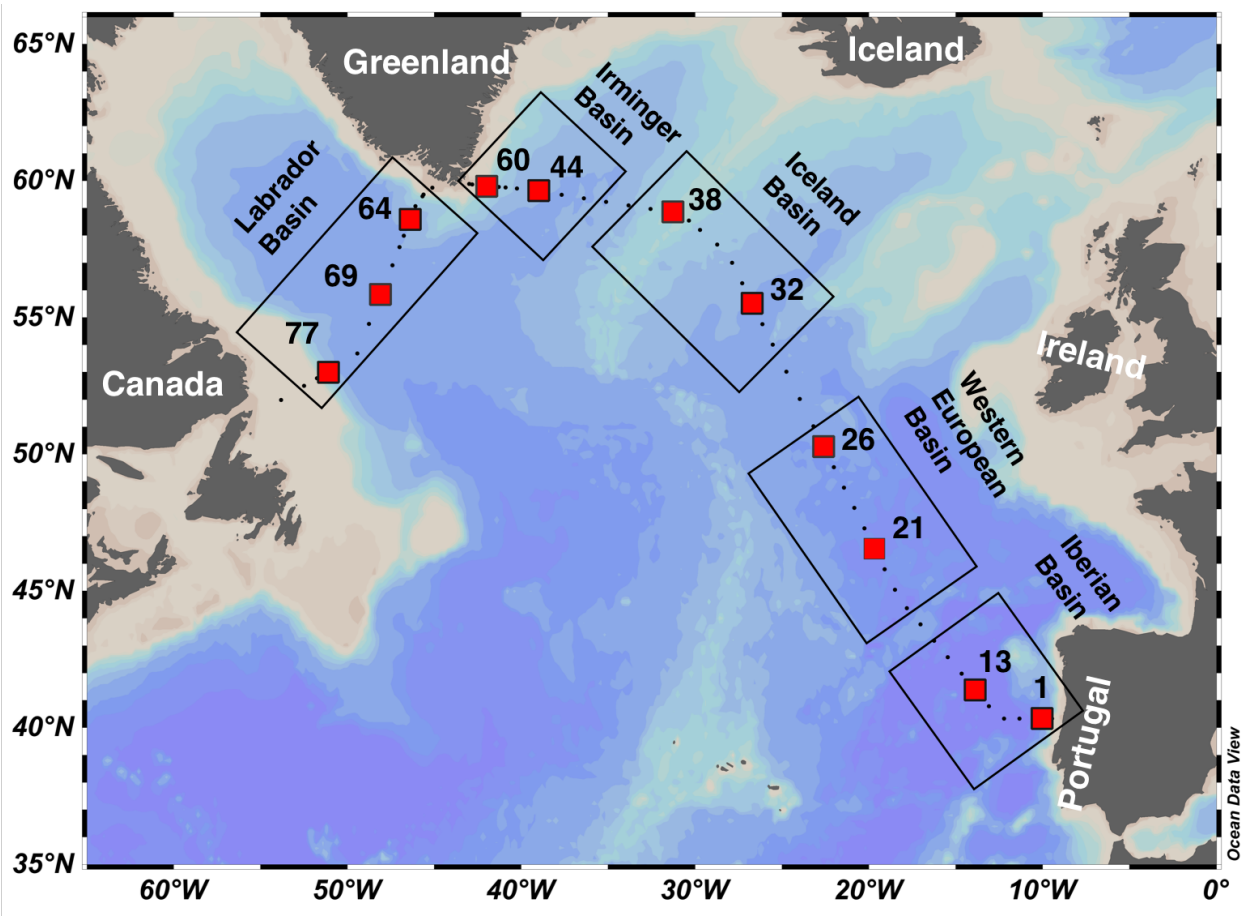


Fig. 1. Map of stations occupied during the GA01 transect in the North Atlantic. The red squares indicate the stations where $^{210}$Po and $^{210}$Pb activities were measured discussed in this study. The transect is divided into the Iberian Basin (stations 1, 13), the Western European Basin (stations 21, 26), the Iceland Basin (stations 32, 38), the Irminger Basin (stations 44, 60), and the Labrador Basin (stations 64, 69, 77).

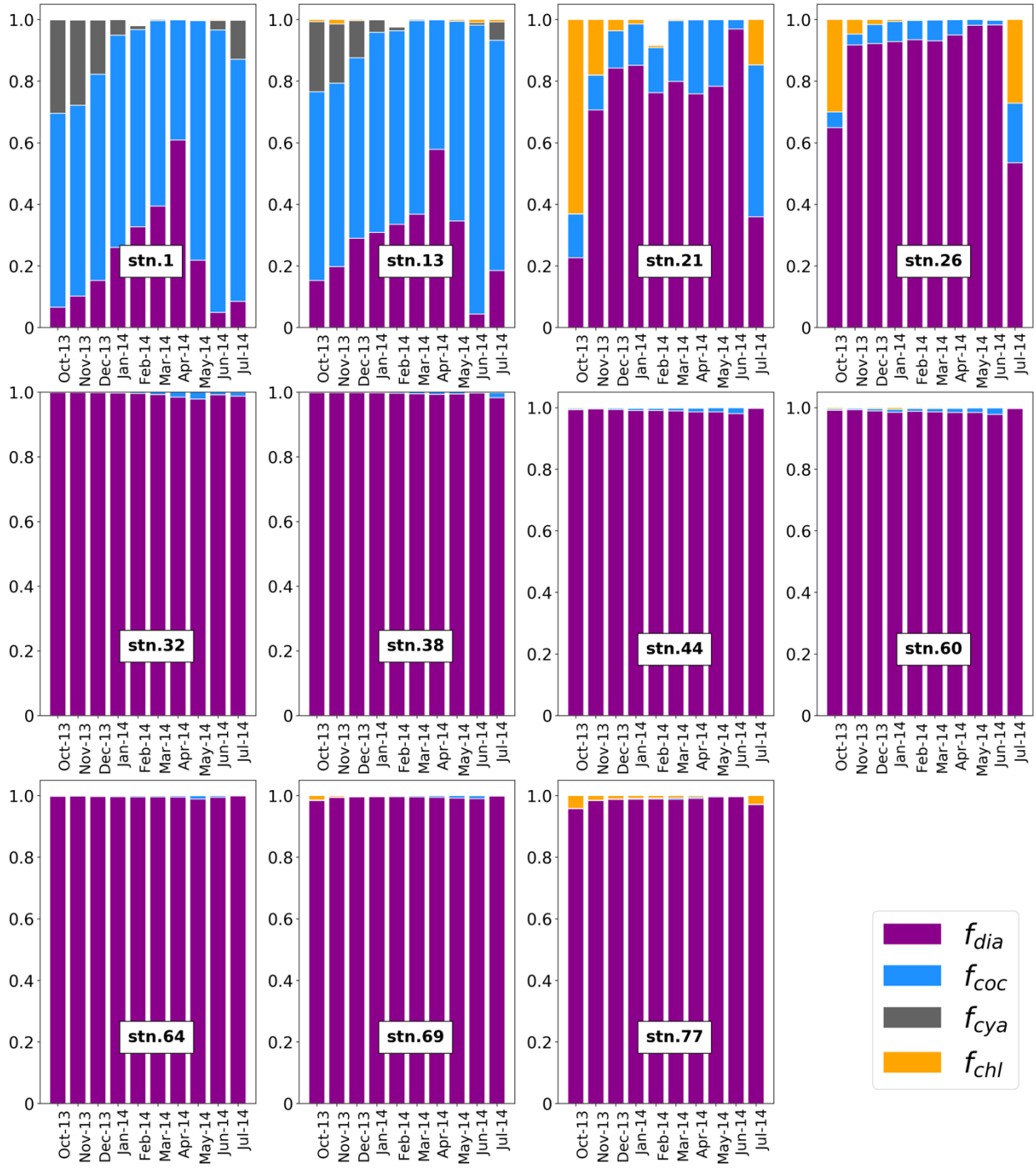


Fig. 2. Satellite-derived monthly average fraction of major phytoplankton groups from October 2013 to July 2014 along the GA01 transect: $f_{dia}$, $f_{coc}$, $f_{cya}$, and $f_{chl}$ are the fraction of diatoms (purple), coccolithophores (blue), cyanobacteria (gray), and chlorophytes (orange), respectively. Data are from the Giovanni online data system https://giovanni.gsfc.nasa.gov/giovanni/.

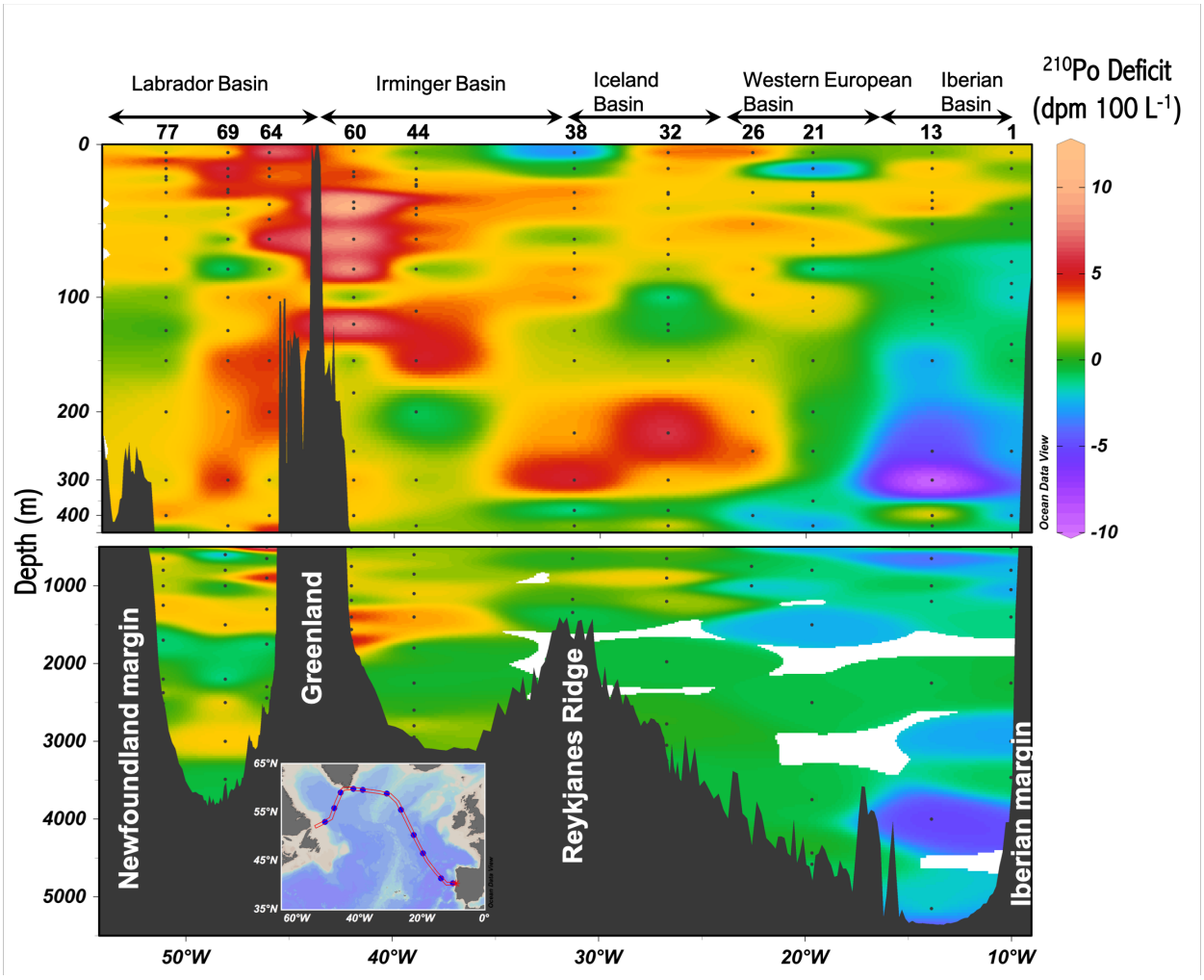


Fig. 3. Section plots of water column $^{210}$Po deficits (dpm 100 L$^{-1}$, total $^{210}$Pb activity minus total $^{210}$Po activity) across the GA01 transect. Upper panel is the upper 500 m. Lower panel is 500 – 5500 m. Station numbers and basins are shown on the top of the upper panel.

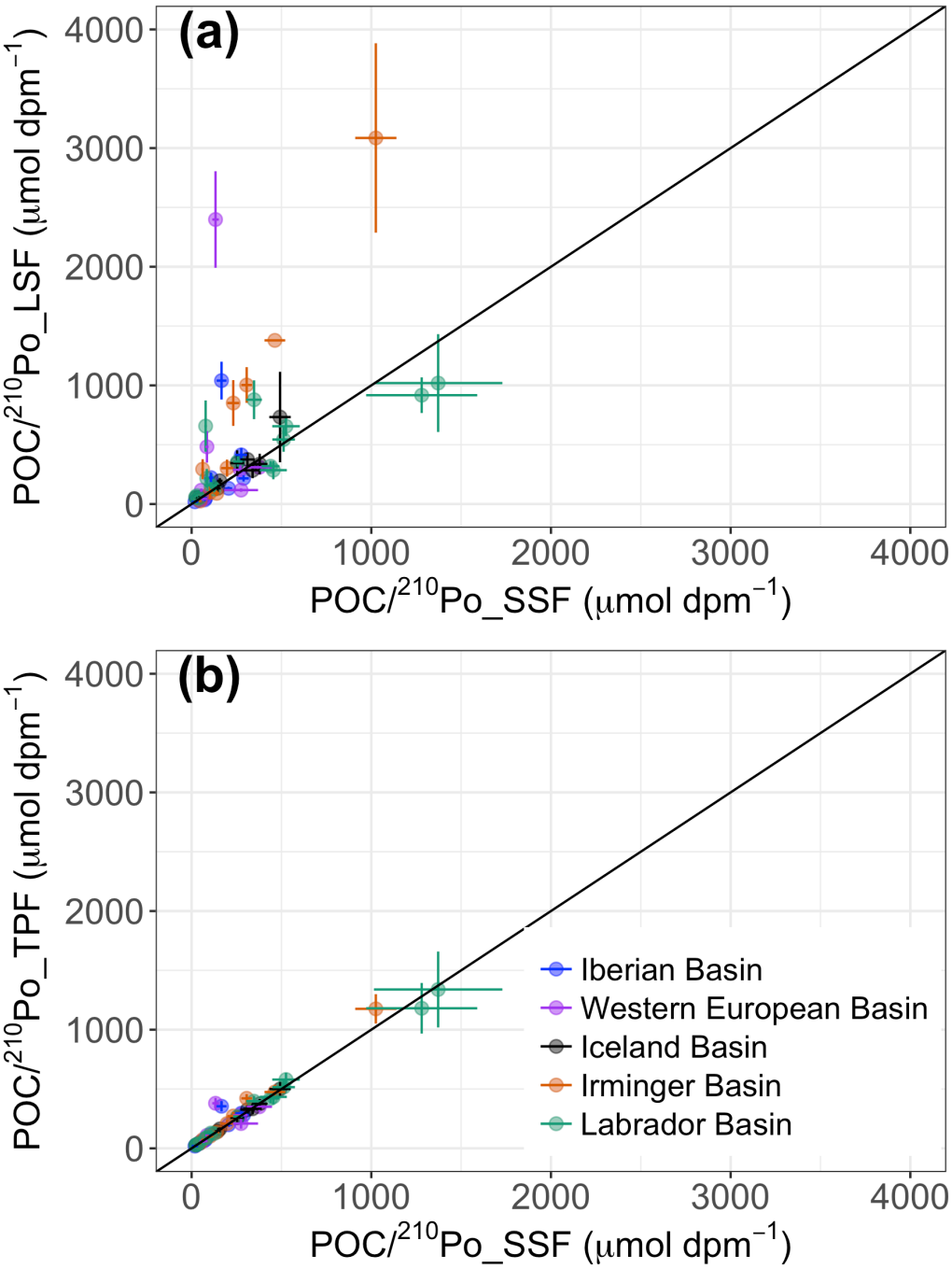


Fig. 4. Plots of the ratios of POC concentration to $^{210}$Po activity in: (a) the large (> 53 μm) particles (POC/$^{210}$Po_LSF) against the small (1-53 μm) particles (POC/$^{210}$Po_SSF), and in (b) the total (> 1 μm) particles (POC/$^{210}$Po_TPF) against the small particles. The black lines indicate the 1:1 line.

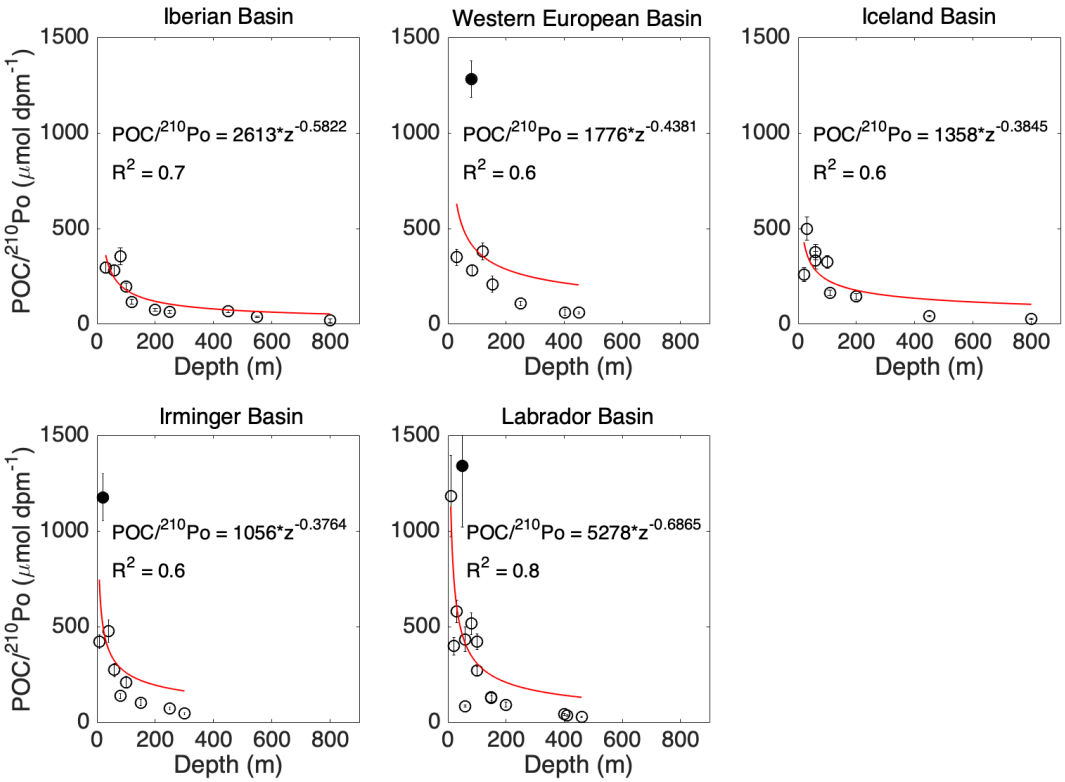


Fig. 5. The ratios of POC concentration to $^{210}$Po activity in the total particles vs. depth in each basin along the GA01 transect. Power law regression (red line) was fitted for POC/ $^{210}$Po against depth in each plot: the Iberian Basin (stations 1, 13), West European Basin (stations 21, 26), Iceland Basin (stations 32, 38), Irminger Basin (stations 44, 60), and Labrador Basin (stations 64, 69, 77). The data points denoted as filled black circles were outliers (points at a distance greater than 1.5 standard deviations from the power law model) and excluded from the power law regression.

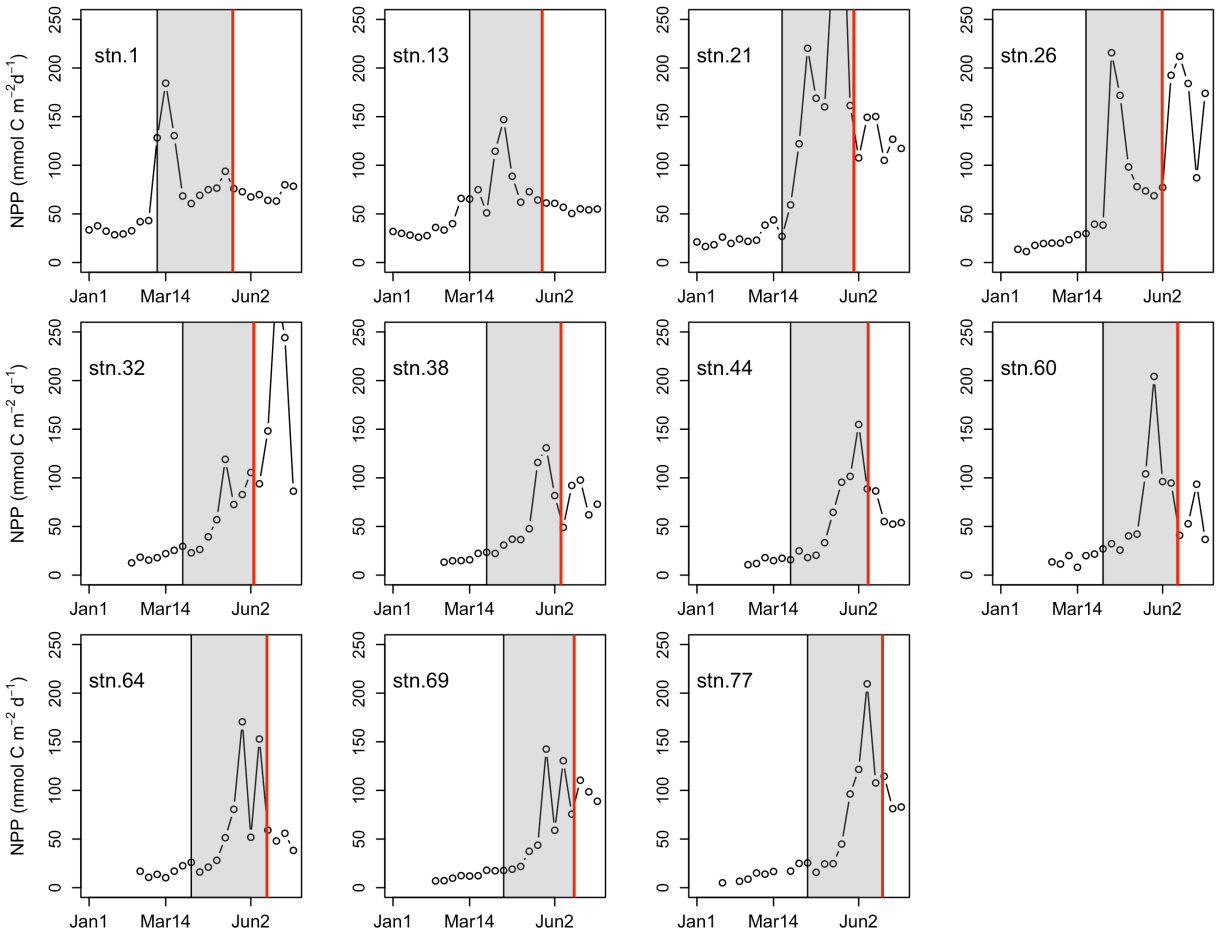


Fig. 6. Time-series (January 1- July 12, 2014) satellite estimates of net primary production (NPP) between January 1 and July 12 in 2014 at each station along the GA01 transect (~~NPP,~~ VPGM algorithm, http://www.science.oregonstate.edu/ocean.productivity/). The shading rectangle in each plot denotes NPP for about 2 months prior to the sampling date. Two months NPP data is needed because such a time scale could ensure the sensitivity for NSS estimates (Friedrich and Rutgers van der Loeff, 2002; Stewart et al., 2007). The vertical red line in each plot indicates the sampling date at each station.

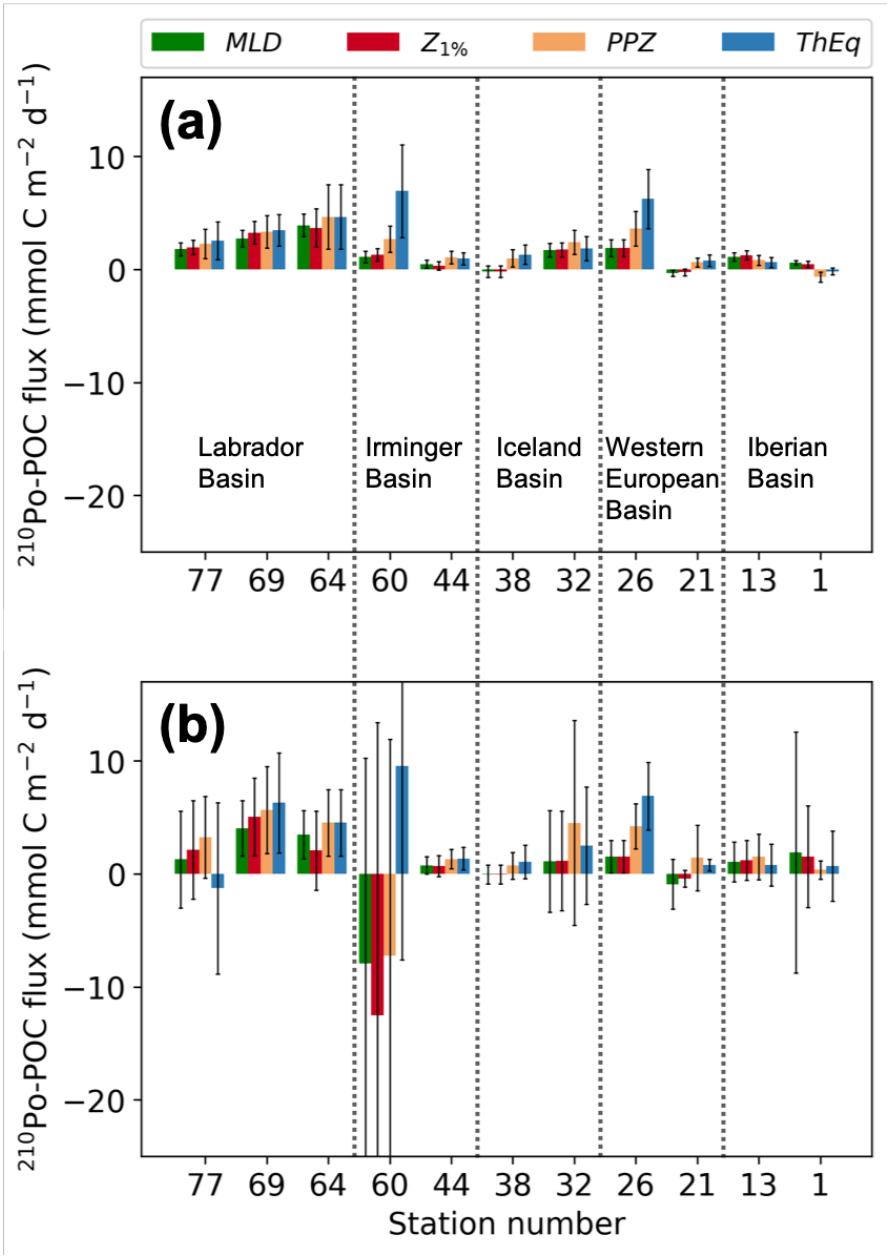


Fig. 7. POC fluxes derived from $^{210}$Po for the mixed layer depth (MLD), the base of the euphotic zone ($Z_{1\%}$), the base of the primary production zone (PPZ), and the $^{234}$Th-$^{238}$U equilibrium depth (ThEq). (a) POC fluxes derived from the $^{210}$Po fluxes that were calculated from the deficit alone; (b) POC fluxes derived from the sum of the $^{210}$Po fluxes that were calculated from the $^{210}$Po deficit and vertical advective flux. Note that the > 1 μm particles were used to calculate the POC/$^{210}$Po ratios. The stations were plotted from west to east.

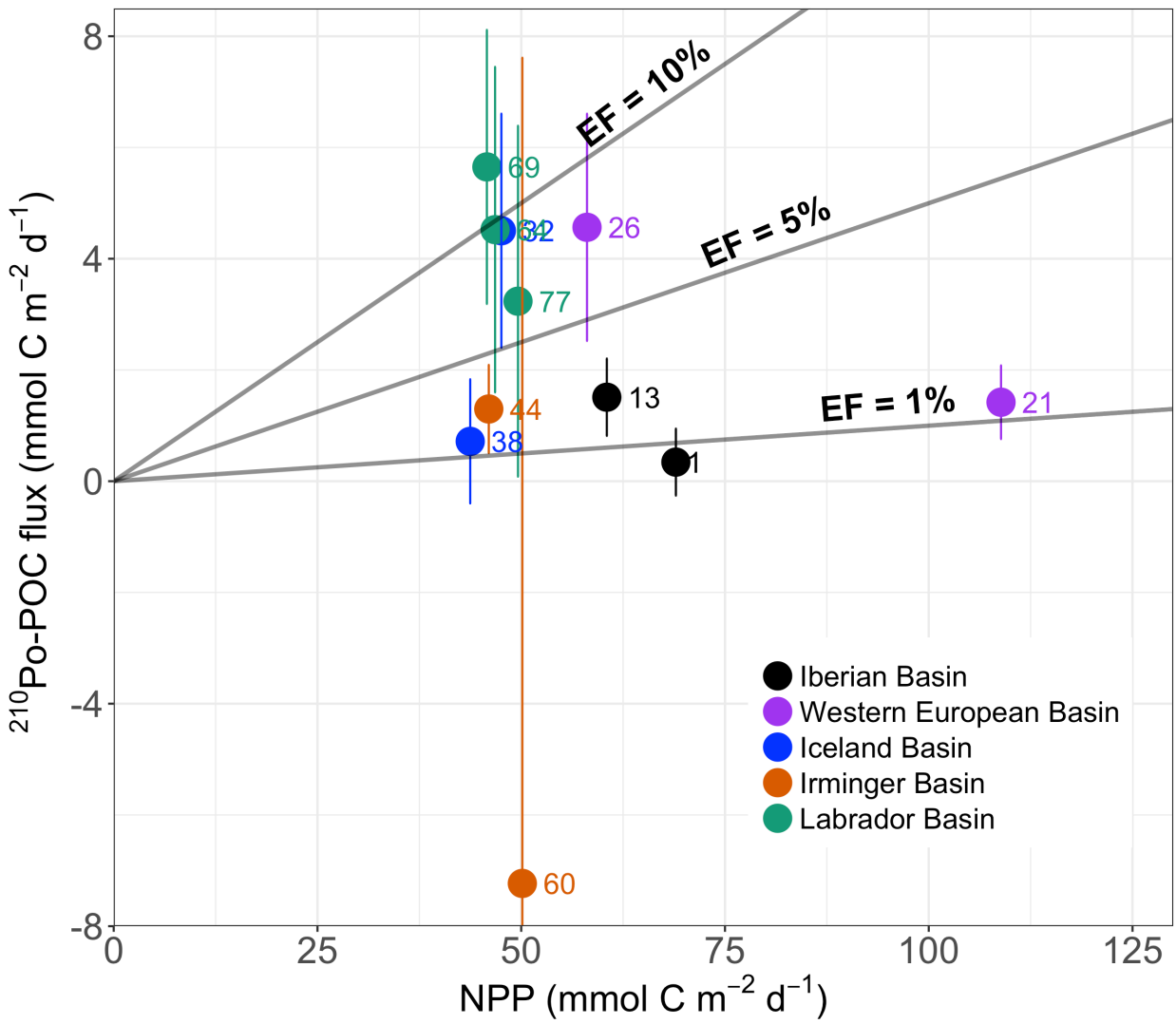


Fig. 8. Plot of POC export flux derived from $^{210}$Po method ($^{210}$Po-POC) versus satellite estimates of net primary production (NPP). The NPP values were averaged for the previous 138 days ($^{210}$Po half-life) prior to the sampling date. The sum of the $^{210}$Po fluxes calculated from the $^{210}$Po deficit and vertical advective flux, and the POC/$^{210}$Po ratios in the > 1 μm particles were used to derive POC fluxes. The $^{210}$Po-POC fluxes were integrated within the primary production zone (PPZ). Lines of export efficiency (EF) of 10%, 5%, and 1% are drawn in the plot. The numbers in the plot are labelled as station numbers. The color codes of the stations correspond to the basins.

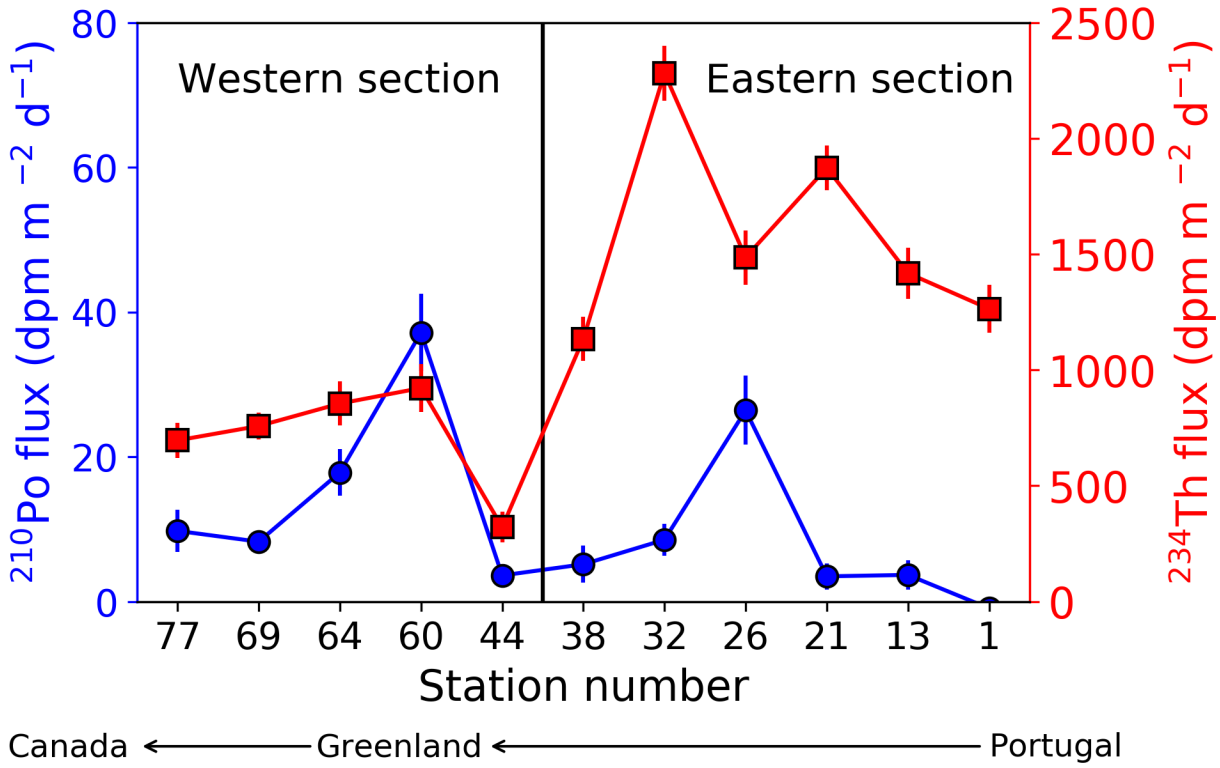


Fig. 9. Sinking fluxes of $^{210}$Po (blue circles) and $^{234}$Th (red squares) integrated to the depth where $^{234}$Th activity returned to equilibrium with $^{238}$U activity (ThEq) assuming steady state and negligible physical transport along the GA01 transect. Note that the stations are plotted from west to east, and the transect was separated into the western (stations 44 - 77) and eastern (stations 1 - 38) sections.

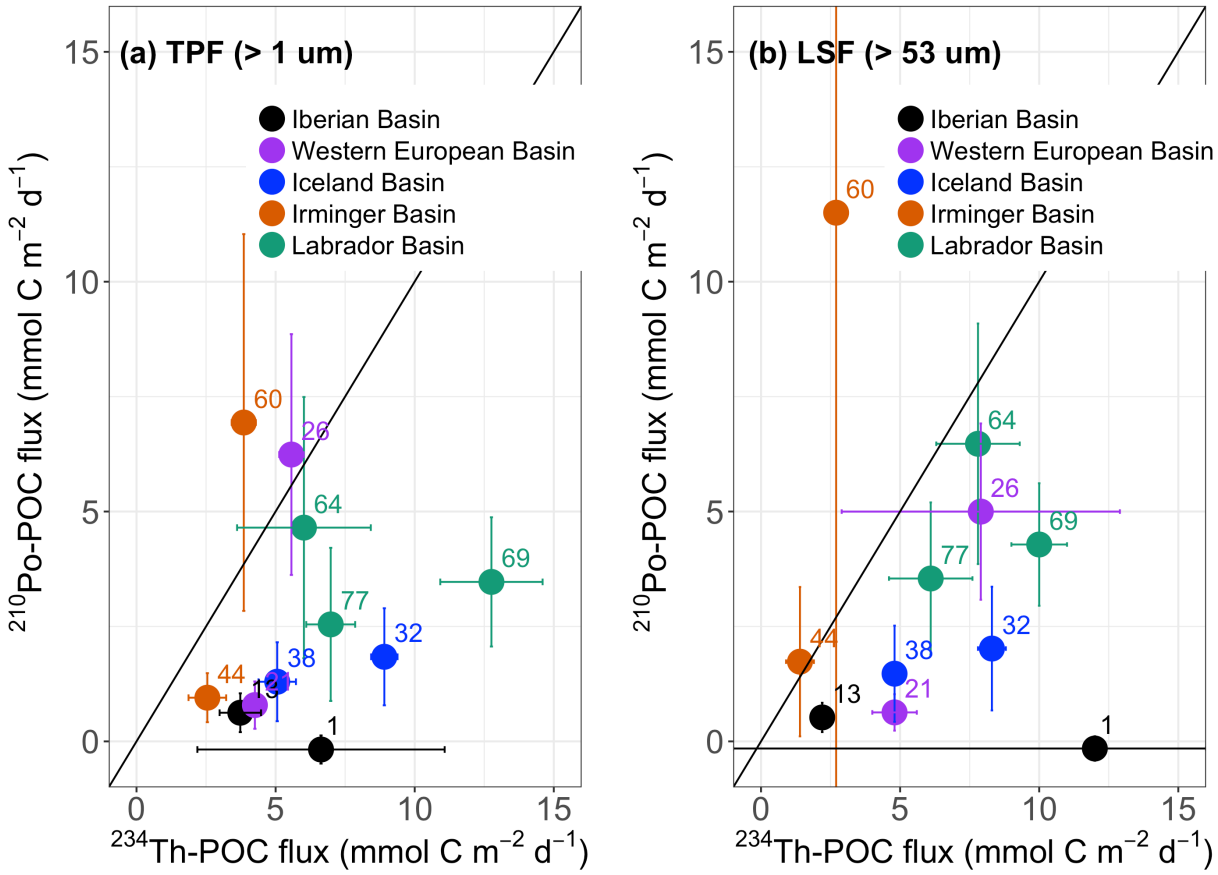


Fig. 10. Plot of the POC flux derived from $^{210}$Po ($^{210}$Po-POC) versus the POC flux derived from $^{234}$Th ($^{234}$Th-POC) at 11 stations along the GA01 transect. Both the fluxes of $^{210}$Po and $^{234}$Th were calculated from the deficit term alone assuming steady state and negligible physical transport. The POC/radionuclide ratios on (a) total particulate fraction (TPF, > 1 μm) and (b) large size fraction (LSF, > 53 μm) were used to calculate the POC flux. The fluxes were integrated down to the depth where $^{234}$Th activity returned to equilibrium with $^{238}$U activity (ThEq). The numbers in the plot are station numbers. The color codes of the stations correspond to the basins.